

Universal recording of immune cell interactions in vivo

<https://doi.org/10.1038/s41586-024-07134-4>

Received: 18 April 2023

Accepted: 30 January 2024

Published online: 6 March 2024

 Check for updates

Sandra Nakandakari-Higa¹, Sarah Walker^{2,3,14}, Maria C. C. Canesso^{1,4,14}, Verena van der Heide^{5,6,7}, Aleksey Chudnovskiy¹, Dong-Yoon Kim⁴, Johanne T. Jacobsen^{1,13}, Roham Parsa⁴, Jana Bilanovic¹, S. Martina Parigi⁸, Karol Fiedorczuk⁹, Elaine Fuchs^{8,10}, Angelina M. Bilate⁴, Giulia Pasqual¹¹, Daniel Mucida^{4,10}, Alice O. Kamphorst^{5,6,7}, Yuri Pritykin^{2,12} & Gabriel D. Victora¹✉

Immune cells rely on transient physical interactions with other immune and non-immune populations to regulate their function¹. To study these ‘kiss-and-run’ interactions directly *in vivo*, we previously developed LIPSTIC (labelling immune partnerships by SorTagging intercellular contacts)², an approach that uses enzymatic transfer of a labelled substrate between the molecular partners CD40L and CD40 to label interacting cells. Reliance on this pathway limited the use of LIPSTIC to measuring interactions between CD4⁺ T helper cells and antigen-presenting cells, however. Here we report the development of a universal version of LIPSTIC (uLIPSTIC), which can record physical interactions both among immune cells and between immune and non-immune populations irrespective of the receptors and ligands involved. We show that uLIPSTIC can be used, among other things, to monitor the priming of CD8⁺ T cells by dendritic cells, reveal the steady-state cellular partners of regulatory T cells and identify germinal centre-resident T follicular helper cells on the basis of their ability to interact cognately with germinal centre B cells. By coupling uLIPSTIC with single-cell transcriptomics, we build a catalogue of the immune populations that physically interact with intestinal epithelial cells at the steady state and profile the evolution of the interactome of lymphocytic choriomeningitis virus-specific CD8⁺ T cells in multiple organs following systemic infection. Thus, uLIPSTIC provides a broadly useful technology for measuring and understanding cell–cell interactions across multiple biological systems.

Physical interactions in which cells exchange signals through membrane-bound molecules are at the core of multiple tissue functions^{3,4}. In the immune system such interactions feature prominently, from the priming of T cells by dendritic cells (DCs) that initiates the adaptive immune response to the CD4⁺ T cell help that enables B cells to produce high-affinity antibodies^{1,5}. More recent work has explored the role of interactions between immune and non-immune cells, such as those forming the epithelial barrier of the gut and skin, which are thought to drive transcriptional changes in immune cells that in turn enable them to support tissue function^{6,7}. Despite their importance, cell–cell interactions have traditionally been directly observed only by microscopy⁸, which has the key limitation that interacting cells cannot be retrieved for downstream analysis. Thus, the impact of the interaction on cell behaviour and the cellular features that lead the interaction to occur in the first place cannot be inferred from traditional imaging alone. More recently, spatial transcriptomics and high-density imaging

technologies have allowed for more in-depth characterization of the states of cells in the same neighbourhood⁹. However, even when capable of high resolution, transcriptomic and imaging techniques still report on proximity between cells rather than on true physical interaction and signal exchange between membranes, requiring additional indirect methods and assumptions to infer functional interactions computationally (for example, ref. 10). High-throughput identification of cellular interactors and full deconvolution of the transcriptomic effects of physical interaction on cellular behaviour and function are therefore yet to be achieved.

Many such limitations can be overcome by proximity-based labelling across cellular membranes^{2,11–16}. These approaches rely on equipping ‘donor’ cells with enzymes or other signals that act over short distances to identify ‘acceptor’ cells in either close proximity or physical contact. An early example was our development of LIPSTIC, which uses enzymatic labelling across immune synapses

¹Laboratory of Lymphocyte Dynamics, The Rockefeller University, New York, NY, USA. ²Lewis-Sigler Institute for Integrative Genomics, Princeton University, Princeton, NJ, USA. ³Department of Quantitative and Computational Biology, Princeton University, Princeton, NJ, USA. ⁴Laboratory of Mucosal Immunology, The Rockefeller University, New York, NY, USA. ⁵Marc and Jennifer Lipschultz Precision Immunology Institute, Icahn School of Medicine at Mount Sinai, New York, NY, USA. ⁶Tisch Cancer Center, Icahn School of Medicine at Mount Sinai, New York, NY, USA. ⁷Department of Oncological Sciences, Icahn School of Medicine at Mount Sinai, New York, NY, USA. ⁸Laboratory of Mammalian Cell Biology and Development, The Rockefeller University, New York, NY, USA. ⁹Laboratory of Membrane Biology and Biophysics, The Rockefeller University, New York, NY, USA. ¹⁰Howard Hughes Medical Institute, The Rockefeller University, New York, NY, USA. ¹¹Laboratory of Synthetic Immunology, Department of Surgery, Oncology and Gastroenterology, University of Padova, Padua, Italy. ¹²Department of Computer Science, Princeton University, Princeton, NJ, USA. ¹³Present address: Institute for Immunology and Transfusion Medicine, Rikshospitalet, University of Oslo, Oslo, Norway. ¹⁴These authors contributed equally: Sarah Walker, Maria C. C. Canesso. [✉]e-mail: pritykin@princeton.edu; victora@rockefeller.edu

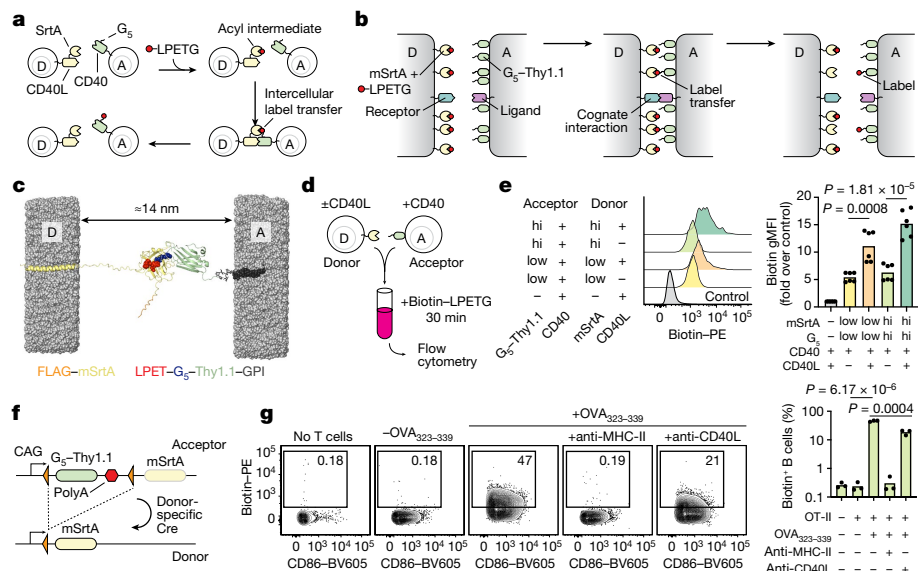


Fig. 1 | The uLIPSTIC system. **a,b**, Schematic comparison of the original LIPSTIC² (**a**) and the uLIPSTIC (**b**) systems. In the original system (**a**), SrtA and G₅ were brought into proximity by fusion to a receptor–ligand pair involved in a cell–cell interaction, allowing intercellular transfer of labelled substrate (LPETG) from the donor (D) cell to the acceptor (A) cell. In uLIPSTIC (**b**), SrtA and G₅ (fused to the irrelevant protein Thy1.1) are anchored nonspecifically to the cell membrane at high density; the enzymatic reaction is allowed to proceed when apposing membranes come within a short distance (<14 nm) of each other, which can be driven by interactions between any receptor–ligand pair of the appropriate dimensions. **c**, Computational model depicting the intermembrane span of fully extended mSrtA following transfer of the LPETG substrate onto G₅-Thy1.1. **d**, Populations of 293T cells co-transfected with high or low levels of either mSrtA or G₅-Thy1.1 were co-incubated in the presence of biotin–LPETG for 30 min and analysed by flow cytometry. **e**, Histograms showing the extent of labelling of acceptor cells following the treatment in **d**.

Each symbol on the column plot represents one technical replicate, pooled from two independent experiments. gMFI, geometric mean fluorescence intensity. **f**, The Rosa26^{uLIPSTIC} mouse allele. Using the Ai9 high-expression backbone²⁰, a loxP (orange triangles)-flanked G₅-Thy1.1 coding sequence is followed by mSrtA coding sequence. Cre recombinase switches cells from 'acceptor' (G₅-Thy1.1) to 'donor' (mSrtA) mode. **g**, Rosa26^{uLIPSTIC/+}.CD4-Cre OT-II donor T cells were co-cultured with Rosa26^{uLIPSTIC/+} acceptor B cells in the presence or absence of OVA₃₂₃₋₃₃₉ peptide and blocking antibodies to CD40L and MHC-II. The flow cytometry plots (left), gated on B cells, show biotin–LPETG transfer from T to B cells and numbers indicate the percent of B cells in the gated population. Each symbol in the column plot (right) represents a biological replicate from three independent experiments. For **e,g**, *P* values were calculated using two-tailed Student's *t*-tests. The graphics in **a** and **d** were adapted from ref. 2.

to directly record cell–cell interactions *in vivo*². In its first iteration, LIPSTIC labelled only interactions delivered through CD40 and CD40L, which restricted its utility to interactions involving effector CD4⁺ T cells. Here we report the development of uLIPSTIC, which enables us to record interactions between an extended array of cell types, regardless of the surface molecules involved. Coupling uLIPSTIC to standard single-cell RNA sequencing (scRNA-seq) methods allows for atlas-type characterization of the 'cellular interactome' of a population of interest and for the definition of the molecular pathways associated with such interactions. Thus, uLIPSTIC enables us to achieve truly quantitative interaction-based transcriptomics without the need for computational inference of transcriptomes or interacting molecules.

Universal recording of cell interactions

LIPSTIC uses the *Staphylococcus aureus* transpeptidase sortase A (SrtA) to covalently transfer a peptide substrate containing the motif LPETG onto an amino-terminal pentaglycine (G₅) acceptor². In its original version, catalysis by the very low-affinity (about 1.8 mM) interaction between LPETG-loaded SrtA and its G₅ target^{17,18} was favoured by genetically fusing each component to one of the members of a receptor–ligand pair², thus raising the local concentration of the reactants above the threshold required for substrate transfer (Fig. 1a). We reasoned that a similarly high local concentration of enzyme and target could also be achieved in a 'universal' receptor–ligand-independent manner by driving very high levels of expression of SrtA and G₅ on apposing cell membranes without direct fusion to the interacting molecules,

potentially providing a readout for physical interactions between cells of any type (Fig. 1b).

To test this, we generated a donor–acceptor pair consisting of the 'PDK' version of SrtA¹⁷ targeted to the plasma membrane by fusion to the human PDGFRB transmembrane domain² (mSrtA) and the G₅ peptide fused to the N terminus of the mouse Thy1.1 GPI-anchored protein. Three-dimensional modelling (Fig. 1c) predicted the maximal distance between membranes at which label transfer would occur to be approximately 14 nm, comparable to the intermembrane span required, for example, for the interaction between the T cell receptor (TCR) and the major histocompatibility complex (MHC; about 15 nm), and narrower than the typical distance separating juxtaposed cell membranes in the absence of receptor–ligand interactions, set by glycocalyx repulsion¹⁹. Given the negligible affinity (about 1.8 mM) between LPETG-loaded SrtA and G₅ (ref. 17), such a design would in principle allow for label transfer only when cells were functionally interacting at a close intermembrane distance, without driving artificial interactions between its engineered components. We transfected HEK293T cells with high or low concentrations of plasmids expressing either mSrtA or G₅-Thy1.1, adding biotin–LPETG substrate to combined cell populations as described previously² (Fig. 1d). Label transfer was detectable above background when donor and acceptor populations were forced to interact by co-transfection of constructs encoding CD40L and CD40, respectively, and further increased when the uLIPSTIC components were transfected at the highest concentration (Fig. 1e). Thus, a high level of expression of SrtA and G₅ on the membrane allows LIPSTIC labelling in the absence of fusion to specific receptor–ligand pairs.

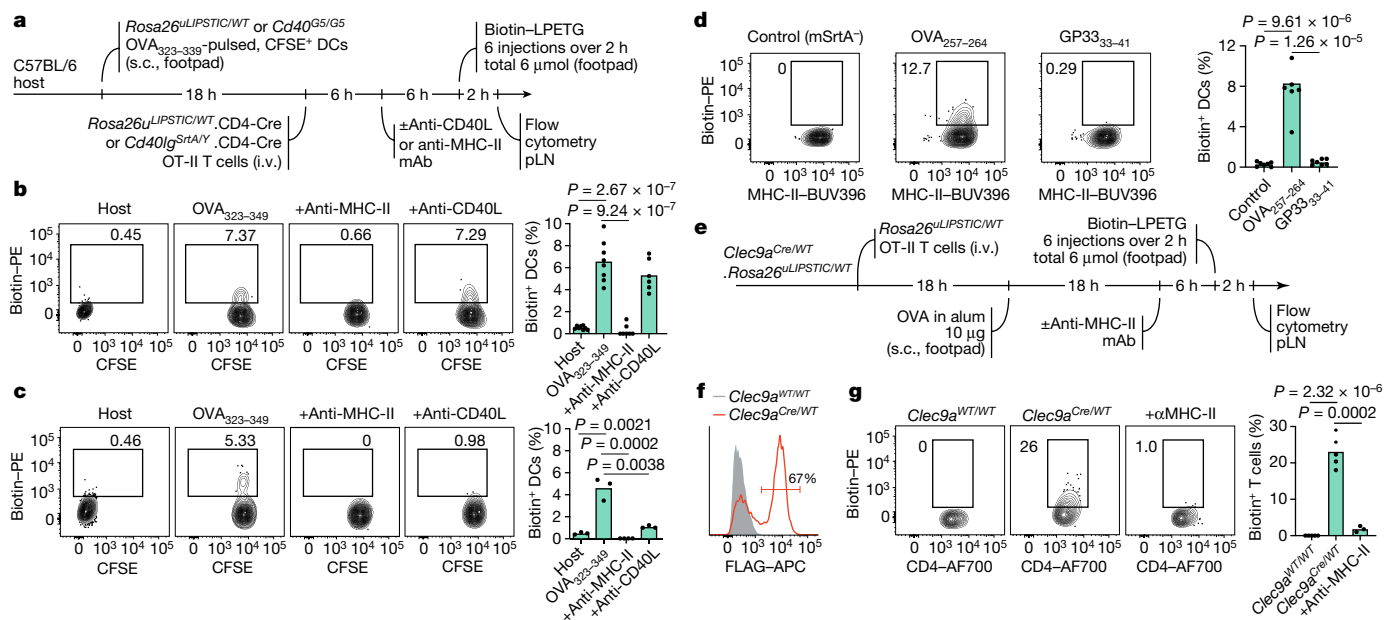


Fig. 2 | uLIPSTIC labelling of cell–cell interactions in vivo. **a**, Experimental workflow for the experiments in **b,c**. s.c., subcutaneous; mAb, monoclonal antibody. **b,c**, uLIPSTIC (**b**) and CD40L LIPSTIC (**c**) labelling of adoptively transferred DCs in an in vivo priming model. The flow cytometry plots (left) are gated on transferred (CFSE-labelled) DCs. The column plot on the right summarizes the extent of DC labelling. **d**, uLIPSTIC labelling of DCs by CD8⁺ T cells. Experimental setup as in **a**, but DCs were pulsed either with cognate (OVA₂₅₇₋₂₆₄) or control (LCMV GP33₃₃₋₄₁) peptides and transferred along with Rosa26^{uLIPSTIC/WT}.CD4-Cre OT-ICD8⁺ donor T cells or control mSrtA⁻

Rosa26^{uLIPSTIC/WT} OT-ICD8⁺ T cells. Labelling of DCs is summarized in the column plot. **e–g**, Labelling of antigen-specific CD4⁺ T cells by Clec9a-expressing DCs. **e**, Experimental workflow. i.v., intravenous. **f**, Efficiency of recombination as percent FLAG-mSrtA-expressing cells in migratory DCs by Clec9a^{Cre/+}. **g**, Left: labelling of adoptively transferred OT-II T cells following immunization with OVA in alum. Right: summary of data. All results shown in column plots are from two independent experiments, with each symbol representing one mouse. Numbers in all flow plots indicate the percentage of cells in the gated population. *P* values were calculated using two-tailed Student's *t*-tests.

We generated a Rosa26^{uLIPSTIC} mouse allele in which a high level of expression of mSrtA (preceded by a Flag tag) or G₅-Thy1.1 was driven by the strong promoter cytomegalovirus early enhancer, chicken β-actin and rabbit β-globin (CAG) introduced into the ubiquitously expressed Rosa26 locus²⁰ (Fig. 1f and Extended Data Fig. 1a). The G₅-Thy1.1 is flanked by loxP sites, so that Cre-mediated recombination leads to expression of a previously silent downstream mSrtA coding sequence, switching Cre-expressing cells from uLIPSTIC acceptors into uLIPSTIC donors (Extended Data Fig. 1d). To test this system, we crossed Rosa26^{uLIPSTIC} mice to the CD4-Cre and OT-II TCR transgenes to generate mSrtA⁺ uLIPSTIC donor T cells specific for peptide 323–339 of the model antigen chicken ovalbumin (OVA). Efficient transfer of labelled substrate between co-cultured T and B cells occurred only in the presence of OVA_{323–339} (Fig. 1g). Substrate transfer was abrogated by addition of a blocking antibody to MHC class II (MHC-II), necessary for the cognate B cell–T cell interaction, but not by an antibody to CD40L (Fig. 1g). Loading of donor T cells positive for mSrtA and its transfer onto G₅-Thy1.1 acceptor DCs increased progressively in the first 2 h of labelling, after which it plateaued (Extended Data Fig. 2a–e). Gradually decreasing peptide–MHC concentration or the affinity of the complex towards the OT-II TCR using truncated altered peptide ligands as described previously^{21,22} led to reduced labelling of DCs in vitro (Extended Data Fig. 2f,g). We conclude that uLIPSTIC enables trans-synaptic labelling of contacts between immune cells regardless of which receptor(s) and ligand(s) drive these interactions.

uLIPSTIC labelling in vivo

To test uLIPSTIC labelling in vivo, we used a well-established T cell priming model^{8,23}, in which G₅-Thy1.1⁺ DCs loaded with OVA_{323–339} are injected into the footpads of mice followed by adoptive transfer of mSrtA⁺ OT-II T cells. Lymphatic migration of DCs to the draining

popliteal lymph node (pLN) allows DC–T cell interactions to take place at this site (Fig. 2a). Footpad injection of biotin–LPETG substrate 24 h after T cell transfer led to detectable labelling of on average 6.5% of transferred DCs (Fig. 2b). Comparable numbers were obtained when using the original CD40L–CD40 LIPSTIC system² (Fig. 2c). Treatment with anti-MHC-II before substrate injection blocked labelling in both settings (whereas treatment with anti-CD40L blocked transfer only by the original LIPSTIC), indicating that the uLIPSTIC components alone are insufficient to artificially drive interactions between neighbouring cells also in vivo. Thus, uLIPSTIC labelling is equivalent to receptor–ligand-specific LIPSTIC for recording the binding patterns of CD4⁺ T cells and DCs in an in vivo priming setting. Pulsing DCs with OVA_{323–339} altered peptide ligands showed that the fraction of labelled DCs decreased as peptide–MHC affinity for the OT-II TCR decreased (Extended Data Fig. 2h–j). Transferring decreasing numbers of mSrtA⁺ donor T cells also decreased the degree to which interacting DCs were labelled (Extended Data Fig. 3a–e). Last, increasing the time interval between substrate administration and tissue collection led to a gradual decrease in biotin detection on the surface of acceptor cells, so that little substrate was detectable 4–6 h after the last injection of substrate (Extended Data Fig. 3f–i). Therefore, uLIPSTIC signal detection is useful for acute but not long-term tracking of interacting cells.

We next used uLIPSTIC to record T cell–DC interactions that were inaccessible to the original LIPSTIC system, either because they do not involve the CD40L–CD40 interaction or because directionality is reversed. mSrtA⁺ OT-I CD8⁺ T cells labelled on average 8.3% of DCs pulsed with their cognate peptide (OVA_{257–264}) but only background levels (0.5%) of DCs pulsed with the lymphocytic choriomeningitis virus (LCMV) GP33_{33–41} peptide (Fig. 2d). Inverting the uLIPSTIC reaction so that endogenous mSrtA⁺ DCs (in Rosa26^{uLIPSTIC/+}.Clec9a^{Cre/+} mice, in which most DCs are labelled due to Clec9a expression in common DC progenitors²⁴) labelled adoptively transferred Rosa26^{uLIPSTIC/+} OT-II CD4⁺

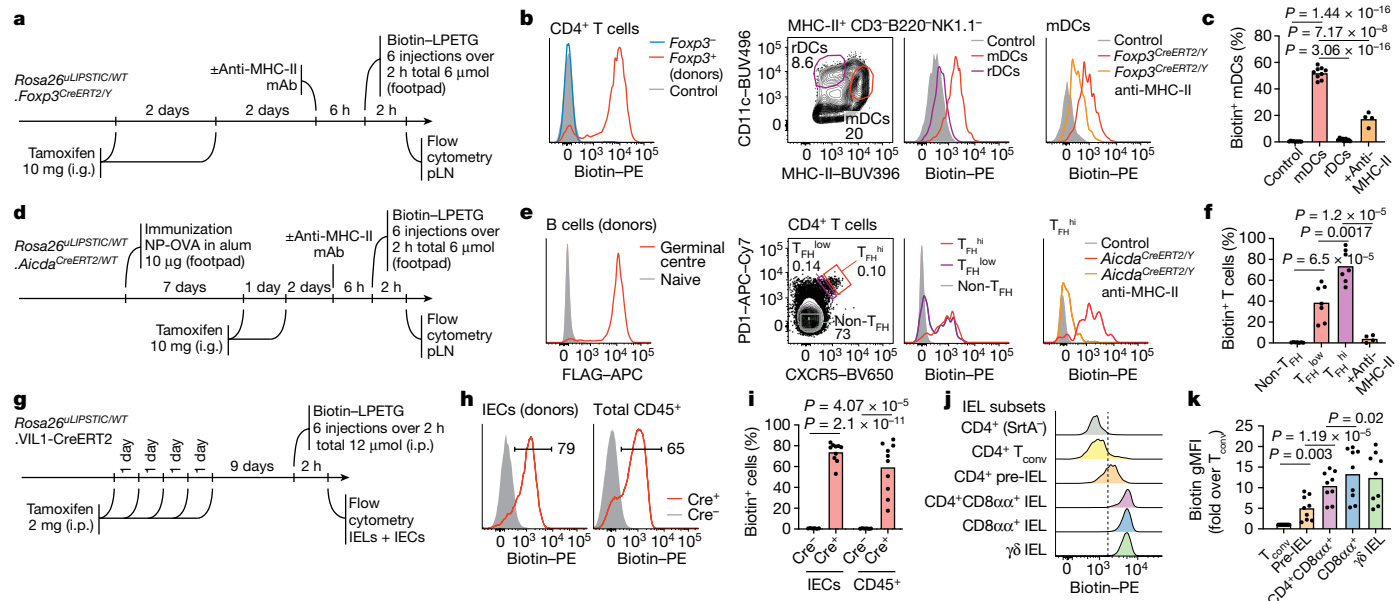


Fig. 3 | uLIPSTIC identifies cellular partners of T_{reg} cells, T_{FH} cells and IECs.

a, Experimental workflow for **b,c**, i.g., intragastrically. **b**, Left: efficiency of recombination of the uLIPSTIC allele in T_{reg} cells by $Foxp3^{CreERT2}$. The biotin signal represents the acquisition of substrate by T_{reg} cells (the biotin-labelled LPET-loaded SrtA acyl intermediate) and also shows the absence of transfer of substrate to $Foxp3^-$ T cells. Centre: labelling of migratory DCs (mDCs) and resident DCs (rDCs) by T_{reg} cells at the steady state. Right: labelling of mDCs following injection of a blocking antibody to MHC-II. **c**, Summary of data from three independent experiments. **d**, Experimental workflow for **e,f**. **e**, Labelling of T_{FH} cells by germinal centre B cells. Left: efficiency of recombination of the uLIPSTIC allele in germinal centre B cells by $Aicda^{CreERT2}$ after two doses of tamoxifen, as in **b**. Centre: labelling of T_{FH} cells by germinal centre B cells at 10 days after immunization with NP-OVA in alum. T cells are gated as those with

high or low levels of expression of the T_{FH} markers CXCR5 and PD1 (T_{FH}^{hi} and T_{FH}^{low} , respectively). Right: labelling of T_{FH}^{hi} cells following injection of a blocking antibody to MHC-II. **f**, Summary of data from two independent experiments. **g**, Experimental workflow for **h–k**. **h**, Left: efficiency of conversion of IECs into uLIPSTIC donors and substrate capture in VIL1-CreERT2 mice (as in **b**). Right: labelling of total CD45⁺ intraepithelial leukocytes. **i**, Summary of data from three independent experiments. **j**, Differential labelling of selected IEL populations by IEC donors. The dashed line is placed for reference. **k**, Summary of biotin geometric mean fluorescence intensity from three independent experiments. For all column plots, each symbol represents one mouse; bars represent the mean. Numbers in all flow plots and histograms indicate the percent of cells in the gated population. *P* values were calculated using two-tailed Student's *t*-tests.

T cells following OVA immunization (Fig. 2e–g) led to detectable labelling of roughly 22% of transferred T cells (likely because of incomplete recombination of donor conventional DC subset 2 cells by $Clec9a^{Cre}$; Extended Data Fig. 1e). Labelling was again fully abrogated by prior injection of a blocking antibody to MHC-II (Fig. 2f,g). Thus, uLIPSTIC can label interactions between T cells and DCs bidirectionally.

To test uLIPSTIC in settings other than naive T cell priming, we first determined the identity of the cellular partners of regulatory T (T_{reg}) cells in the steady-state LN, using the $Foxp3^{CreERT2}$ driver²⁵ to achieve tamoxifen-dependent recombination of *Rosa26^{uLIPSTIC}* specifically in T_{reg} cells (Fig. 3a,b). Broad characterization of biotin-positive acceptors showed that DCs are the primary population engaged by T_{reg} cells at the steady state, with a smaller contribution from macrophages (Extended Data Fig. 4a). Closer examination of the DC population showed pronounced labelling of most DCs with the migratory (MHC-II^{hi}CD11c^{int}) phenotype, whereas labelling of resident (MHC-II^{int}CD11c^{hi}) DCs was markedly lower (Fig. 3b,c). Labelling of CD8⁺ T cells and $Foxp3^-$ CD4⁺ T cells was negligible in this setting, confirming that simple co-localization of these populations with donor T_{reg} cells within the same microenvironment is not sufficient to drive label transfer (Fig. 3b, left and Extended Data Fig. 4a). Expression of mSrtA in roughly equivalent numbers of T_{reg} cells or total conventional CD4⁺ T cells (the latter achieved by low-dose tamoxifen administration to *Rosa26^{uLIPSTIC/+}*.CD4-CreERT2 mice²⁶) (Extended Data Fig. 4b,c) resulted in much less efficient labelling of migratory-phenotype DCs by conventional T cells (Extended Data Fig. 4d). Thus, interaction with migratory-phenotype DCs at the steady state, although not a unique property of T_{reg} cells, is more pronounced among this subset. T_{reg} cell labelling of migratory-phenotype DCs was decreased

but not completely abrogated by administration of a blocking antibody to MHC-II, confirming that the interaction between these two populations is partly driven by the TCR–MHC-II axis but suggesting that other receptor–ligand pairs may also contribute to this process (Fig. 3b,c).

We next determined the phenotype of the T cells that provide help to B cells in germinal centres, which can be difficult to identify unambiguously using the canonical T follicular helper (T_{FH}) cell markers CXCR5 and PD1 (ref. 27). We immunized *Rosa26^{uLIPSTIC/+}*. $Aicda^{CreERT2/+}$ mice²⁸ in the footpads with the model antigen 4-hydroxy-3-nitro-phenylacetyl (NP)-OVA to generate germinal centres, and then treated these mice with tamoxifen 7 and 8 days later to induce mSrtA expression in germinal centre B cells (Fig. 3d). Germinal centre B cells replaced G₅-Thy1.1 with mSrtA much faster than did resting CD4⁺ T cells, indicating that replacement kinetics vary across donor populations (Extended Data Fig. 4e–g). Biotin-LPETG injection 10 days post-immunization led to substantial labelling of CXCR5^{hi}PD1^{hi} T_{FH} acceptor cells but not CXCR5^{PD1^{int}} non- T_{FH} cells in the pLN (Fig. 3e,f). Only a fraction of CXCR5^{int}PD1^{int} T cells were labelled by germinal centre B cells, indicating that relatively few of the cells in this population are indeed engaged with germinal centre B cells. Again, blocking of MHC-II led to total loss of T_{FH} cell labelling, confirming the specificity of the reaction (Fig. 3e,f).

Last, we sought to test the ability of uLIPSTIC to record interactions between immune and non-immune cells outside secondary lymphoid organs. Intraperitoneally (i.p.) injected LIPSTIC substrate reaches donor cells in multiple organs in mice (including brain, bone marrow, kidney, lungs, spleen and thymus), and its use is therefore not limited to draining LNs (Extended Data Fig. 5). As a test case, we measured substrate transfer from intestinal epithelial cells (IECs) to the intraepithelial

T lymphocytes (IELs) that reside within this compartment²⁹. We crossed *Rosa26^{uLIPSTIC}* mice to villin 1 (VILI)-CreERT2 mice³⁰ to generate IEC donors following tamoxifen treatment (Fig. 3g). i.p.-administered biotin-LPETG was transferred efficiently onto a large fraction (median 65%) of CD45⁺ IELs (Fig. 3h,i and Extended Data Fig. 6a,b). Labelling followed a gradient corresponding to the stage of differentiation of these cells: whereas ‘natural’ TCR $\gamma\delta$ ⁺ and CD8 $\alpha\alpha^+$ TCR $\alpha\beta^+$ IELs exhibited uniformly high uLIPSTIC signal, labelling among induced CD4⁺ IELs³¹ followed closely their developmental trajectory^{6,32}, from background levels in the CD4⁺CD8 $\alpha\alpha^-$ CD103⁻ ‘conventional’ (T_{conv}) subset to intermediate labelling in CD4⁺CD8 $\alpha\alpha^-$ CD103⁺ pre-IELs and levels comparable to those of natural IELs in the epithelium-adapted CD4⁺CD8 $\alpha\alpha^+$ CD103⁺ population (Fig. 3j,k). Thus, uLIPSTIC is capable of recording interactions between epithelial and immune cells in the small intestine.

We conclude that uLIPSTIC can be used to label a wide variety of immune cell interactions *in vivo* across multiple organs, both in adoptive transfer and in fully endogenous models. In the latter, uLIPSTIC revealed the interaction preferences of steady-state LNT_{reg} cells, identified populations of T_{FH} cells capable of providing help to B cells in the germinal centre, and showed stepwise acquisition by intraepithelial CD4⁺ T cells of the ability to physically interact with IECs.

uLIPSTIC-based transcriptomics

A key feature of uLIPSTIC is its ability to identify the full cellular interactome of a given cell type in an unbiased manner. Reading out this interactome is best achieved by scRNA-seq, which is also unbiased in its ability to identify labelled cell populations. As LIPSTIC labelling has a wide dynamic range², coupling it to scRNA-seq also has the potential to identify genes and transcriptional programs quantitatively associated with the degree of interaction between two cell types, which can in principle reveal the molecular pathways that drive a given interaction (Fig. 4a). To explore these possibilities, we labelled *Rosa26^{uLIPSTIC/WT}*. VILI-CreERT2 mice as in Fig. 3g. Sorted CD45⁺ cells (enriched for rarer leukocyte populations as in Extended Data Fig. 6c) stained with a DNA-barcoded anti-biotin antibody were then profiled by droplet-based scRNA-seq using the 10X Genomics platform. Immune cell populations were identified by marker gene expression and TCR reconstruction and by comparison with publicly available gene signatures (Fig. 4b, Extended Data Figs. 6d–k, 7 and 8 and Supplementary Tables 1 and 2). uLIPSTIC revealed broad variation in the extent to which different populations interacted with IECs, which aligned with the data obtained by flow cytometry. The level of labelling was high among natural IELs (TCR $\gamma\delta$ and TCR $\alpha\beta^+$ CD8 $\alpha\alpha^+$), low or negligible among B cell subsets, and intermediate in plasmacytoid DCs (Fig. 4b,c). uLIPSTIC also labelled two less clearly defined populations that interacted strongly with IECs, including a small cluster of cells likely to be myeloid cells and a larger cluster marked by a high expression level of genes such as *Atxn1* and *Btbd11* (Fig. 4c and Extended Data Figs. 6d,j,k and 7). CD4⁺ T cells again showed a gradient in their ability to interact with IECs, which became more apparent when these cells were clustered into subpopulations (Fig. 4d, Extended Data Fig. 8a–c and Supplementary Table 3). The ability to acquire the biotin label largely followed a developmental trajectory (determined from gene expression alone) that began with a highly polyclonal naive-like population with low uLIPSTIC signal and followed through a pre-IEL intermediate into a fully differentiated, oligoclonal CD4⁺ IEL state^{6,32} (Fig. 4d–f) labelled to a similar extent as natural IELs (Fig. 4c).

Correlating the uLIPSTIC signal within CD4⁺ T cells with the expression of all detected genes in our dataset (Fig. 4g,h) revealed multiple significant correlations with markers of IEL differentiation. These included negative correlations with naive T cell markers such as *Sell* (encoding for L-selectin) and *Tcf7* and positive correlations with CD4⁺ IEL-associated genes such as *Ccl5*, *Gzma*, *Itgae*, *Itgb7* and *Jaml*⁶ (Fig. 4g,h, Extended Data Fig. 8d,e and Supplementary Table 4). The last three are of particular

interest, given that CD103 (the $\alpha_E\beta_7$ integrin, encoded by *Itgae* and *Itgb7*) and JAML (junction adhesion molecule-like, encoded by *Jaml*) are interacting partners of E-cadherin and of the coxsackie and adenovirus receptor (CAR), respectively, both of which are expressed in the tight junctions of the intestinal epithelium^{33–36}. Flow cytometry confirmed the correlation between biotin acquisition and expression of CD103 (Extended Data Fig. 8f), and *in vivo* staining with an anti-JAML antibody confirmed stepwise acquisition of this molecule during CD4⁺ IEL development (Fig. 4i). Search for correlations among ‘canonical’ (M2, CP) pathways in the MSigDB database³⁷ revealed a significant positive correlation between biotin acquisition by CD4⁺ T cells and expression of genes in the BioCarta cytotoxic T lymphocyte pathway, among others (Extended Data Fig. 8g). Targeted correlation analysis showed strong positive and negative correlations (|Spearman’s ρ | > 0.75) between biotin acquisition and expression of genes modulated as conventional T cells develop into CD4⁺ IELs⁶ (Fig. 4j, Extended Data Fig. 8h,i and Supplementary Table 5). We conclude that uLIPSTIC allows for quantitative interaction-based transcriptomics, enabling us not only to define the cellular interactomes of populations of interest, but also to discern specific genes and signatures associated with acquisition of the ability to form specific cell–cell interactions.

Applying uLIPSTIC to LCMV infection

Finally, we investigated the interacting partners of virus-specific CD8⁺ T cells in a classic systemic infection model, using the Armstrong strain of LCMV³⁸. We infected uLIPSTIC acceptor (*Rosa26^{uLIPSTIC/WT}*) mice that had previously received CD8⁺ uLIPSTIC donor T cells carrying the LCMV-specific P14 TCR (*Rosa26^{uLIPSTIC/+}.CD4-Cre.P14-tg*) with LCMV by the i.p. route. We administered LIPSTIC substrate to these mice at different time points before collecting the mediastinal LN (mLN), a focal point of the early immune response in this model³⁹ (Fig. 5a and Extended Data Fig. 9a). uLIPSTIC detected the expected engagement of P14 T cells with DCs as early as 36 h post-infection (hpi), which peaked at 50 hpi and then declined by 96 hpi (Fig. 5b). However, DCs accounted for an average of only 5.4% of the full P14 cellular interactome at all time points analysed (Fig. 5c and Extended Data Fig. 9b), suggesting that other populations in addition to DCs may contribute to the initial activation of LCMV-specific CD8⁺ T cells. uLIPSTIC-coupled single-cell transcriptomics identified most P14-interacting cells at 36 hpi as monocytic lineage cells, potentially monocytes (Mo) or macrophages (MΦ) expressing high levels of *Ly6c2* (‘Mo/MΦ1’ cluster; Fig. 5d–f, Extended Data Fig. 9d–j and Supplementary Table 6). Following a phase of broader uLIPSTIC labelling spread evenly across most mLN populations at 50 hpi, the P14 interactome at 96 hpi became enriched in a second cluster of monocytic cells expressing lower levels of *Ly6c2* and higher levels of *H2-Aa* (the ‘Mo/MΦ2’ cluster, comprising either a distinct population of macrophages or a further differentiation stage of *Ly6c2*^{hi} monocytes⁴⁰; Fig. 5d–f and Extended Data Fig. 9d–j). Flow cytometry of uLIPSTIC-labelled cells confirmed this transition: whereas P14 interactors in the monocyte and macrophage gate (F4/80⁺MHC-II^{low-int}) consisted almost entirely of *Ly6c*^{hi}MHC-II⁺ monocytes at 36 hpi, this population shifted markedly towards a *Ly6c*^{int}MHC-II^{int} phenotype at the 96 hpi time point (Fig. 5g). To determine whether these interactions were antigen dependent, we compared labelling between mice infected with wild-type (WT) LCMV or with a mutant lacking the P14 epitope (LCMV(ΔP14))⁴¹. Whereas uLIPSTIC labelled a large fraction of monocytic lineage cells in mice infected with WT LCMV, such labelling was completely absent from LCMV(ΔP14)-infected mice at all time points (Fig. 5h). Thus, the interactions between CD8⁺ T cells and monocyte lineage cells revealed by uLIPSTIC are antigen dependent, suggesting that the latter may acquire and present viral antigen *in vivo* at early time points after LCMV infection.

We also profiled the interactomes of P14 CD8⁺ T cells in the liver, lung and spleen at 96 hpi, when accumulation of donor cells becomes evident

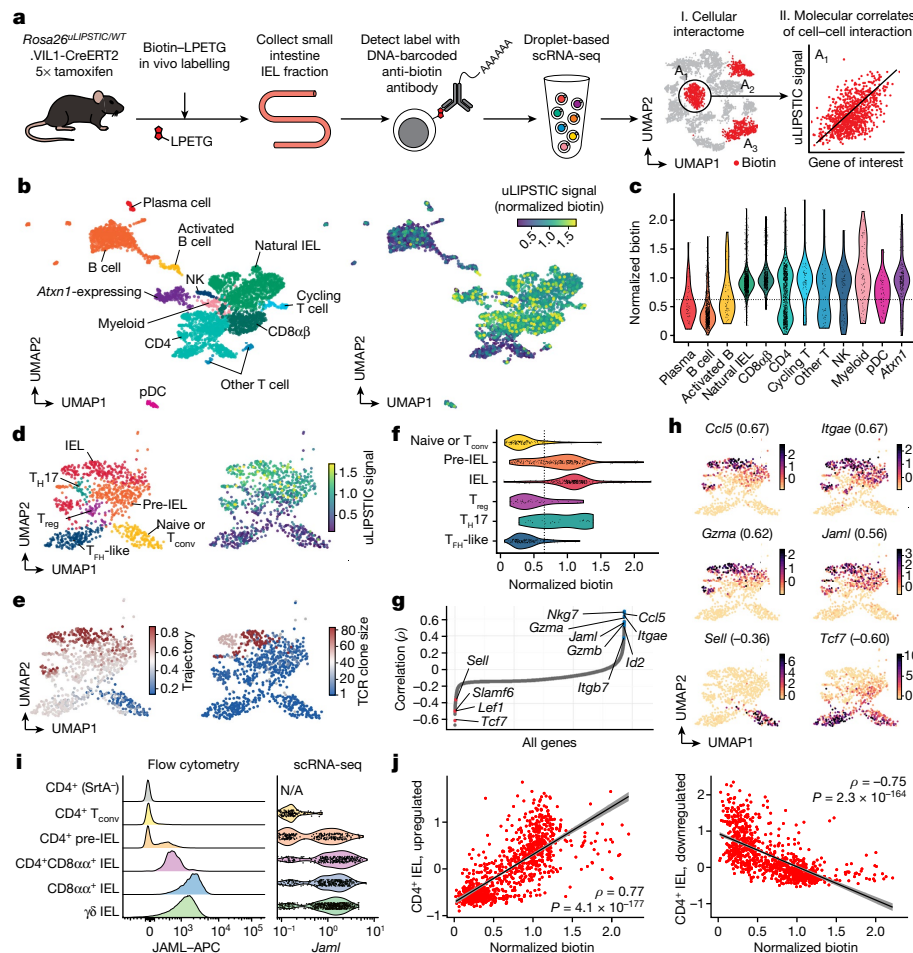


Fig. 4 | Using uLIPSTIC for interaction-based transcriptomics.

a, Experimental workflow. **b**, Uniform manifold approximation and projection (UMAP) plots of the CD4⁺ intraepithelial immune cell fraction from a uLIPSTIC reaction as in Fig. 3g. Data are pooled from three mice. Left: main cell populations (see Extended Data Figs. 6 and 7). NK, natural killer; pDC, plasmacytoid DC. Right: normalized uLIPSTIC signal in log-scaled arbitrary units. **c**, Normalized uLIPSTIC signal among CD4⁺ cell populations. The dotted line represents the threshold for cells to be considered acceptors, based on overall distribution of normalized biotin. **d**, UMAP plots of CD4⁺ T cells from **b**, $n = 915$ cells. Left: main cell subpopulations (see Extended Data Fig. 8). Right: normalized uLIPSTIC signal. **e**, Inferred trajectory (left) and $\alpha\beta$ TCR diversity (plotted as clone size; right) among CD4⁺ T cells. **f**, Normalized uLIPSTIC signal among CD4⁺ T cell subpopulations. **g**, Correlation (Spearman's ρ) between normalized uLIPSTIC signal and normalized gene expression, calculated for each gene over all CD4⁺

T cells, shown in order of increasing correlation. Selected significantly correlated genes (false discovery rate $<1 \times 10^{-23}$) are highlighted. **h**, Normalized expression of selected genes. Correlation with normalized uLIPSTIC is shown in parentheses. **i**, Representative samples showing in vivo staining of JAML in IELs and scRNA-seq expression of *Jaml* in the equivalent populations. In the latter, CD8 $\alpha\alpha$ ⁺ and $\gamma\delta$ IEL were separated from within the 'Natural IEL' cluster by the presence of rearranged $\alpha\beta$ TCRs or expression of the *Trdc* gene. **j**, Relationship between normalized uLIPSTIC signal among all CD4⁺ T cells and expression of gene signatures upregulated and downregulated as epithelial T cells transition from T_{conv} (CD4⁺CD103⁺CD8 $\alpha\alpha$ ⁺) to CD4⁺ IEL (CD4⁺CD103⁺CD8 $\alpha\alpha$ ⁺) phenotypes (signatures based on data from ref. 6). The trend line and error are for linear regression with 95% confidence interval; Spearman's ρ and two-sided P value are listed.

by flow cytometry (not shown). As with mLNs, interactions between P14 T cells and monocytic lineage cells were observed at all three sites (Fig. 5i, Extended Data Fig. 10a–g and Supplementary Table 7). Labelled monocytic cells included a larger cluster that closely matched the Mo/MΦ2 phenotype found in the mLN, as well as a smaller population of cells that resembled Mo/MΦ1 cells, in addition to a further cluster that comprised splenic red-pulp macrophages in the spleen and related populations in liver and lung ('RP MΦ' cluster; Fig. 5i,j and Extended Data Fig. 10d–g). Infection with mutant (LCMV(Δ P14)) virus confirmed that P14 interactions with monocytes or macrophages in all tissues was dependent on the presence of the P14 epitope (Fig. 5k and Extended Data Fig. 10h), again underscoring the ability of uLIPSTIC to detect antigen-dependent interactions. We conclude that the combination of uLIPSTIC and single-cell transcriptomics enables the identification of non-canonical cell–cell interactions even in well-characterized models, revealing a previously unappreciated predominance of monocytic cells

as the primary interaction partners of CD8⁺ T cells in mLN during early systemic LCMV infection.

Discussion

This study describes a generalization of the LIPSTIC method² that does not require cognate interaction between a pre-specified receptor–ligand pair for label transfer, allowing one to probe the full cellular interactome of a population of interest in an unbiased manner. Although most of the experiments we present involve interactions between immune cells, and particularly T cells, uLIPSTIC is in principle applicable to any population of cells that interact physically with each other. However, whereas labelling in our original cognate system² reports on the engagement of a pre-defined pathway, the nature and function of interactions revealed by uLIPSTIC must be determined downstream, on a case-by-case basis. uLIPSTIC, especially when

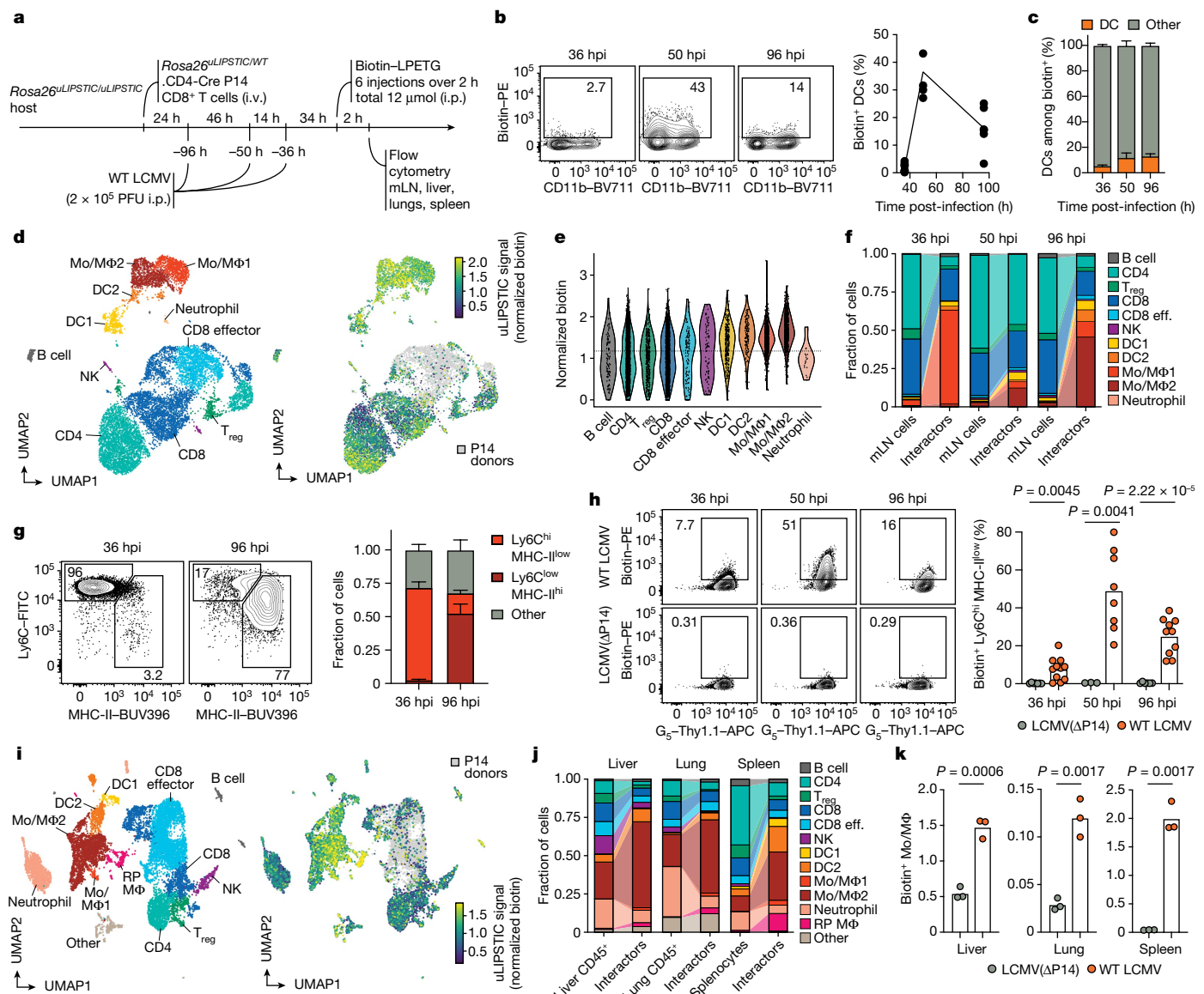


Fig. 5 | Using uLIPSTIC to dissect the early events in CD8⁺ T cell priming following LCMV infection. **a**, Experimental workflow. PFU, plaque-forming units. **b**, Left: labelling of DCs by P14 cells at the indicated time point. Right: summary of data for WT LCMV from three independent experiments. **c**, Proportion of DCs among biotin-positive acceptor cells, as determined by flow cytometry. Data for six mice per time point from three independent experiments are shown. **d**, UMAP plots of mLN cells sorted as in **a**. Data are pooled from 36, 50 and 96 hpi, with 2–3 mice per time point. Cells were enriched for uLIPSTIC acceptors and depleted of B cells as described in Extended Data Fig. 9c. Left: main cell type annotations (see Extended Data Fig. 9g–i). Right: normalized uLIPSTIC signal (biotin), excluding donor P14 cells. **e**, Normalized uLIPSTIC signal among all cell populations, excluding donor P14 cells. The dotted line represents the threshold for cells to be considered acceptors, based on overall bimodal distributions of normalized biotin. **f**, Distribution of cell types as in **d** in total mLN cells versus in the

biotin-positive acceptor fraction (excluding P14 donors). eff., effector. **g**, Left: distribution of uLIPSTIC-labelled monocytic cells (Mo/MΦ) at the indicated time points. Right: abundance of the indicated populations as a fraction of all uLIPSTIC-labelled acceptor cells. Data for four mice per time point from one experiment are shown. **h**, Left: uLIPSTIC labelling of Ly6C^{hi} monocytes (Mo/MΦ) at the indicated time points after infection with either WT LCMV or LCMV(ΔP14). Right: quantification of data from three independent experiments. **i**, As in **d** but for pooled samples from liver, lung and spleen at 96 hpi. RP, red pulp. **j**, As in **f** but for pooled samples from liver, lung, and spleen at 96 hpi. **k**, uLIPSTIC labelling of MHC-II^{hi} monocytes or macrophages (Mo/MΦ²) in organs of mice treated as in **a** but infected with either WT LCMV or LCMV(ΔP14), analysed at 96 hpi. Data from one experiment are shown. Bar plots in **c,g** show mean ± s.e.m. For **b,h,k**, each symbol represents one mouse and *P* values were calculated using two-tailed Student's *t*-test.

coupled to single-cell transcriptomics, is therefore best conceived of as a hypothesis-generating tool.

In the absence of a requirement for cognate interactions, the specificity of uLIPSTIC is ensured by the short intermembrane distance spanned by its components (about 14 nm) and their low intrinsic affinity for each other (millimolar Michaelis constant K_m). Specificity is confirmed experimentally by the findings that: labelling is abrogated by antibodies that block known drivers of the cellular interaction; and not all cells

that are physically juxtaposed label each other, as exemplified by the low degree of labelling of conventional T cells or resident DCs by T_{reg} cell donors. uLIPSTIC thus complements methods such as the use of synthetic Notch receptor variants, which, although they can be used to drive transcription of downstream reporter genes^{13,16}, are based on molecular partners that have high (nanomolar) affinity for each other, and thus are thus themselves capable of driving cellular interactions⁴²; as well as methods based on the spread of cell-permeable labels or

barcoded virions between neighbouring cells by extracellular diffusion^{12,15}, which mark cellular microniches rather than physical interactions between cells. uLIPSTIC has advantages over cell-doublet-based methods⁴³, in that labelling is quantitative rather than binary, and it does not require computational deconvolution of single-cell transcriptional profiles from doublets; however, our system has the relative disadvantage of requiring genetic engineering of its components. Other limitations of uLIPSTIC include the need for relatively high numbers of donor cells to ensure that the true signal is detectable over the noise inherent to flow cytometry, especially when the target acceptor populations are prone to binding detection reagents, as is the case for B cells. Moreover, in acute inflammatory settings, such as in the 50 h time point of LCMV infection (Fig. 5f), labelling appears to broaden to most LN-resident populations, suggesting that non-cognate labelling may occur in altered tissue environments. Again, downstream validation of interactions detected by uLIPSTIC will be critical in such cases.

A central feature of uLIPSTIC is that it can be coupled directly to droplet-based scRNA-seq to achieve quantitative interaction-based transcriptomics. This property can be used in both an ‘atlas’ mode, in which the objective is to identify which populations of acceptor cells interact with a given donor lineage, and in ‘mechanistic’ mode, in which correlations between uLIPSTIC signal intensity and expression of individual genes or gene signatures allow us to establish the molecular basis of an interaction of interest. Using this approach, we show that the ability of CD4⁺ T cells to interact physically with IECs in the small intestine is acquired developmentally as these cells adapt to the intestinal tissue environment and acquire the phenotypic and transcriptional features of CD4⁺ IELs^{6,32,44}. We also show that LCMV infection triggers CD8⁺ T cells to engage in interactions with monocytic cells, which greatly outnumber their interactions with DCs and may thus play a role in cytotoxic T lymphocyte priming. Our findings complement those of a previous study showing the expansion, following acute LCMV infection, of a monocytic population capable of priming CD8⁺ T cells in vitro⁴⁵.

In conclusion, uLIPSTIC provides an unbiased platform for measurement of known cell–cell interactions as well as discovery of new ones. When coupled to scRNA-seq, uLIPSTIC interaction-based transcriptomics has the ability to quantify correlations between the intensity of cell–cell interactions and gene expression, allowing insight into the biology of the interaction itself. We expect this tool will be broadly useful for studying cellular interactions in immunology and beyond.

Online content

Any methods, additional references, Nature Portfolio reporting summaries, source data, extended data, supplementary information, acknowledgements, peer review information; details of author contributions and competing interests; and statements of data and code availability are available at <https://doi.org/10.1038/s41586-024-07134-4>.

1. Dustin, M. L. The immunological synapse. *Cancer Immunol. Res.* **2**, 1023–1033 (2014).
2. Pasqual, G. et al. Monitoring T cell–dendritic cell interactions in vivo by intercellular enzymatic labelling. *Nature* **553**, 496–500 (2018).
3. Greenwald, I. & Rubin, G. M. Making a difference: the role of cell–cell interactions in establishing separate identities for equivalent cells. *Cell* **68**, 271–281 (1992).
4. Sudhof, T. C. & Malenka, R. C. Understanding synapses: past, present, and future. *Neuron* **60**, 469–476 (2008).
5. Victora, G. D. & Nussenzweig, M. C. Germinal centers. *Annu. Rev. Immunol.* **30**, 429–457 (2012).
6. Bilate, A. M. et al. T cell receptor is required for differentiation, but not maintenance, of intestinal CD4⁺ intraepithelial lymphocytes. *Immunity* **53**, 1001–1014 (2020).
7. Niec, R. E., Rudensky, A. Y. & Fuchs, E. Inflammatory adaptation in barrier tissues. *Cell* **184**, 3361–3375 (2021).
8. Mempel, T. R., Henrickson, S. E. & Von Andrian, U. H. T-cell priming by dendritic cells in lymph nodes occurs in three distinct phases. *Nature* **427**, 154–159 (2004).
9. Moses, L. & Pachter, L. Museum of spatial transcriptomics. *Nat. Methods* **19**, 534–546 (2022).
10. Efremova, M., Vento-Tormo, M., Teichmann, S. A. & Vento-Tormo, R. CellPhoneDB: inferring cell–cell communication from combined expression of multi-subunit ligand–receptor complexes. *Nat. Protoc.* **15**, 1484–1506 (2020).
11. Liu, D. S., Loh, K. H., Lam, S. S., White, K. A. & Ting, A. Y. Imaging trans-cellular neuroligin-neuroligin interactions by enzymatic probe ligation. *PLoS ONE* **8**, e52823 (2013).
12. Ombrato, L. et al. Metastatic-niche labelling reveals parenchymal cells with stem features. *Nature* **572**, 603–608 (2019).
13. Zhang, S. et al. Monitoring of cell–cell communication and contact history in mammals. *Science* **378**, eab0503 (2022).
14. Bechtel, T. J., Reyes-Robles, T., Fadeyi, O. O. & Oslund, R. C. Strategies for monitoring cell–cell interactions. *Nat. Chem. Biol.* **17**, 641–652 (2021).
15. Yassin, M. et al. Upregulation of PD-1 follows tumour development in the AOM/DSS model of inflammation-induced colorectal cancer in mice. *Immunology* **158**, 35–46 (2019).
16. Weizman, O. E. et al. Developing synthetic tools to decipher the tumor-immune interactome. *Proc. Natl Acad. Sci. USA* **120**, e2306632120 (2023).
17. Dorr, B. M., Ham, H. O., An, C., Chaikof, E. L. & Liu, D. R. Reprogramming the specificity of sortase enzymes. *Proc. Natl Acad. Sci. USA* **111**, 13343–13348 (2014).
18. Guimaraes, C. P. et al. Site-specific C-terminal and internal loop labeling of proteins using sortase-mediated reactions. *Nat. Protoc.* **8**, 1787–1799 (2013).
19. Dustin, M. L. & Depoil, D. New insights into the T cell synapse from single molecule techniques. *Nat. Rev. Immunol.* **11**, 672–684 (2011).
20. Madisen, L. et al. A robust and high-throughput Cre reporting and characterization system for the whole mouse brain. *Nat. Neurosci.* **13**, 133–140 (2010).
21. Robertson, J. M., Jensen, P. E. & Evavold, B. D. DO11.10 and OT-II T cells recognize a C-terminal ovalbumin 323–339 epitope. *J. Immunol.* **164**, 4706–4712 (2000).
22. Merkenschlager, J. et al. Dynamic regulation of T_H selection during the germinal centre reaction. *Nature* **591**, 458–463 (2021).
23. Stoll, S., Delon, J., Brotz, T. M. & Germain, R. N. Dynamic imaging of T cell–dendritic cell interactions in lymph nodes. *Science* **296**, 1873–1876 (2002).
24. Frederico, B. et al. DNGR-1-tracing marks an ependymal cell subset with damage-responsive neural stem cell potential. *Dev. Cell* **57**, 1957–1975 (2022).
25. Rubtsov, Y. P. et al. Stability of the regulatory T cell lineage in vivo. *Science* **329**, 1667–1671 (2010).
26. Aghajani, K., Keerthivasan, S., Yu, Y. & Gounari, F. Generation of CD4CreER^{T2} transgenic mice to study development of peripheral CD4-T-cells. *Genesis* **50**, 908–913 (2012).
27. Shulman, Z. et al. T follicular helper cell dynamics in germinal centers. *Science* **341**, 673–677 (2013).
28. Dogan, I. et al. Multiple layers of B cell memory with different effector functions. *Nat. Immunol.* **10**, 1292–1299 (2009).
29. McDonald, B. D., Jabi, B. & Bendelac, A. Diverse developmental pathways of intestinal intraepithelial lymphocytes. *Nat. Rev. Immunol.* **18**, 514–525 (2018).
30. el Marjou, F. et al. Tissue-specific and inducible Cre-mediated recombination in the gut epithelium. *Genesis* **39**, 186–193 (2004).
31. Mucida, D. et al. Transcriptional reprogramming of mature CD4⁺ helper T cells generates distinct MHC class II-restricted cytotoxic T lymphocytes. *Nat. Immunol.* **14**, 281–289 (2013).
32. London, M., Bilate, A. M., Castro, T. B. R., Sujino, T. & Mucida, D. Stepwise chromatin and transcriptional acquisition of an intraepithelial lymphocyte program. *Nat. Immunol.* **22**, 449–459 (2021).
33. Cepek, K. L. et al. Adhesion between epithelial cells and T lymphocytes mediated by E-cadherin and the alpha E beta 7 integrin. *Nature* **372**, 190–193 (1994).
34. Zen, K. et al. Neutrophil migration across tight junctions is mediated by adhesive interactions between epithelial coxsackievirus and adenovirus receptor and a junctional adhesion molecule-like protein on neutrophils. *Mol. Biol. Cell* **16**, 2694–2703 (2005).
35. Cohen, C. J. et al. The coxsackievirus and adenovirus receptor is a transmembrane component of the tight junction. *Proc. Natl Acad. Sci. USA* **98**, 15191–15196 (2001).
36. Pazirandeh, A. et al. Multiple phenotypes in adult mice following inactivation of the Coxsackievirus and Adenovirus Receptor (Car) gene. *PLoS ONE* **6**, e20203 (2011).
37. Subramanian, A. et al. Gene set enrichment analysis: a knowledge-based approach for interpreting genome-wide expression profiles. *Proc. Natl Acad. Sci. USA* **102**, 15545–15550 (2005).
38. Oldstone, M. B. et al. Virus and immune responses: lymphocytic choriomeningitis virus as a prototype model of viral pathogenesis. *Br. Med. Bull.* **41**, 70–74 (1985).
39. Olson, M. R., McDermott, D. S. & Varga, S. M. The initial draining lymph node primes the bulk of the CD8 T cell response and influences memory T cell trafficking after a systemic viral infection. *PLoS Pathog.* **8**, e1003054 (2012).
40. Jakubick, C. et al. Minimal differentiation of classical monocytes as they survey steady-state tissues and transport antigen to lymph nodes. *Immunity* **39**, 599–610 (2013).
41. Puglielli, M. T. et al. In vivo selection of a lymphocytic choriomeningitis virus variant that affects recognition of the GP33–43 epitope by H-2Db but not H-2Kb. *J. Virol.* **75**, 5099–5107 (2001).
42. Stevens, A. J. et al. Programming multicellular assembly with synthetic cell adhesion molecules. *Nature* **614**, 144–152 (2022).
43. Giladi, A. et al. Dissecting cellular crosstalk by sequencing physically interacting cells. *Nat. Biotechnol.* **38**, 629–637 (2020).
44. Sujino, T. et al. Tissue adaptation of regulatory and intraepithelial CD4⁺ T cells controls gut inflammation. *Science* **352**, 1581–1586 (2016).
45. Shin, K. S. et al. Monocyte-derived dendritic cells dictate the memory differentiation of CD8⁺ T cells during acute infection. *Front. Immunol.* **10**, 1887 (2019).

Publisher’s note Springer Nature remains neutral with regard to jurisdictional claims in published maps and institutional affiliations.

Springer Nature or its licensor (e.g. a society or other partner) holds exclusive rights to this article under a publishing agreement with the author(s) or other rightsholder(s); author self-archiving of the accepted manuscript version of this article is solely governed by the terms of such publishing agreement and applicable law.

© The Author(s), under exclusive licence to Springer Nature Limited 2024

Methods

Plasmids

All constructs were cloned into the pMP71 vector⁴⁶, which was modified to express a fluorescent reporter (eGFP or tdTomato) followed by the porcine teschovirus 1 self-cleavable 2A peptide⁴⁷ and the protein of interest. The SrtA sequence, including an N-terminal Flag tag, was attached by a single Gly-Gly-Gly-Ser linker⁴⁸ to the human PDGFRB transmembrane domain to form mSrtA. The G_s acceptor sequence was fused at the N terminus of the mouse Thy1.1 protein, downstream of the signal peptide. Sequences of all constructs are included in Supplementary Table 8.

Mice

CD45.2 (C57BL6/J), CD45.1 (B6.SJL *Ptprc*^a), CD4-Cre (ref. 49), CD4-CreERT2 (ref. 49), *Foxp3*^{eGFP-CreERT2} (ref. 25) and *Cx3cr1*^{CreER} mice were purchased from the Jackson Laboratories (strain numbers 000664, 002014, 022071, 022356, 016961 and 020940, respectively). *Clec9a*^{Cre} mice⁵⁰ were a gift from C. Reis e Sousa (Francis Crick Institute, UK), S1pr2-CreERT2 BAC-transgenic mice⁵¹ were generated and provided by T. Kurosaki and T. Okada (Osaka University and RIKEN-Yokohama), and *Aicda*^{CreERT2} mice²⁸ were a gift from Claude-Agnès Reynaud and Jean-Claude Weill (Université Paris-Descartes). OT-II TCR transgenic (Y chromosome)⁵² mice were bred and maintained in our laboratory. The *Rosa26*^{uLIPSTIC} mouse strain was generated by the Rockefeller University Gene Targeting and Transgenics facilities, as described below. All genetically modified strains are bred and maintained under specific-pathogen-free conditions at the Rockefeller University's Comparative Biosciences Center in accordance with institutional guidelines and ethical regulations. P14 TCR transgenic mice specific for LCMV GP_{33–41} on a CD45.1 B6 background were originally provided by Dr R. Ahmed (Emory), maintained at the Icahn School of Medicine at Mount Sinai vivarium, and bred with uLipstic mice. Adult male and female mice of 6–12 weeks of age on the C57BL/6J background were used in all cases. Mice were housed at 72 °F (22.2 °C) and 30–70% humidity in a 12-h light-dark cycle with ad libitum access to food and water. All protocols were approved by the Rockefeller University and Mount Sinai School of Medicine Institutional Animal Care and Use Committees (protocol numbers 22058-H and IACUC-2018-0018/PROTO201900609, respectively).

Generation of the *Rosa26*^{uLIPSTIC} allele

Rosa26^{uLIPSTIC} mice were generated by gene targeting in C57BL/6 embryonic stem cells (ESCs). The *Rosa26*^{uLIPSTIC}-targeting vector is a modification of the Ai9 *Rosa26* conditional expression vector²⁰ (Addgene plasmid No. 22799). G_s-Thy1.1 cDNA preceded by a mouse CD40 signal peptide was inserted into an Nrnl enzyme site in Ai9 immediately downstream of the first *loxP* site, whereas Flag-mSrtA cDNA was introduced in place of the tdTomato gene using FseI enzyme sites. Expression of the cassette in ESCs was screened by standard Southern blotting analysis after EcoRI digestion and using a ³²P probe targeting a sequence near the promoter region, shortly upstream of the left homology arm. Positive ESCs (7.3-kilobase band) were karyotyped, injected into blastocysts and chimeric founders were backcrossed to the C57BL6 background for at least six generations. The full sequences of the uLIPSTIC-targeting vector and the Southern blot probe are reported in Supplementary Table 8. uLIPSTIC mice were deposited at the Jackson Laboratories under strain number 038221.

Isolation of splenic DCs, CD4⁺ T cells and B cells

To isolate DCs, spleens were collected, cut into smaller pieces and incubated for 30 min at 37 °C in HBSS (Gibco) supplemented with CaCl₂, MgCl₂ and collagenase D at 400 U ml⁻¹ (Roche). After digestion, tissue was forced five times through a 21-gauge (G) needle and filtered through a 70-µm strainer into a 15-ml falcon tube with PBS supplemented with

0.5% BSA and 2 mM EDTA (PBE). Red blood cells were lysed with ACK buffer (Gibco), and the resulting cell suspensions were filtered through a 70-µm mesh into PBE. DCs were obtained by magnetic cell separation using anti-CD11c beads (Miltenyi Biotec), as per the manufacturer's instructions. To isolate CD4⁺ T cells and CD8⁺ T cells, spleens were forced through a 70-µm strainer and then ACK-lysed, and the resulting suspension was isolated by negative selection using a cocktail of biotinylated antibodies targeting Ter119, CD11c, CD11b, CD25, B220, NK1.1 and either CD8 (for CD4⁺ isolation) or CD4 (for CD8⁺ isolation), followed by anti-biotin beads (Miltenyi Biotec), as per the manufacturer's instructions. B cells were processed similarly to T cells from the spleens and isolated by negative selection using anti-CD43 beads (Miltenyi Biotec), as per the manufacturer's instructions.

Adoptive cell transfers

For DC transfer experiments, splenic DCs were isolated as described above from mice subcutaneously injected with 1 × 10⁶ B16 melanoma cells that constitutively secrete FMS-like tyrosine kinase 3 ligand (Flt3L)⁵³ 10 days before collection. Cells were resuspended at 10⁷ cells ml⁻¹ and incubated with 10 µM OVA^{323–339}, LCMV GP^{61–80}, OVA^{257–264} or LCMV^{276–286} peptides (Anaspec) in RPMI + 10% FBS, for 30 min at 37 °C. For cell labelling, CFSE or CTV (Thermo Fisher) was added to a final concentration of 2 µM during the last 5 or 20 min of incubation, respectively. Cells were washed three times in RPMI + 10% FBS and resuspended at 2 × 10⁷ cells ml⁻¹ in PBS supplemented with 0.4 µg ml⁻¹ LPS (Sigma-Aldrich). DCs were injected (5 × 10⁵ cells in 25 µl) subcutaneously into the hind footpads. For CD4⁺ T cell and CD8⁺ T cell transfer experiments, 3 × 10⁵ T cells isolated as described above were injected intravenously in 100 µl PBS per mouse. For LCMV infection experiments, 2 × 10⁶ P14 CD8⁺ T cells were transferred intravenously 24 h before infection.

Immunizations

Mice were immunized by subcutaneous injection into the hind footpad with 10 µg OVA or 10 µg NP-OVA (Biogenesis Technologies) adsorbed in alum (Imject Alum, Thermo Fisher) at 2:1 antigen/alum (v/v) ratio in 25 µl volume.

LCMV infections

For acute LCMV infections, mice were injected i.p. with 2 × 10⁵ plaque-forming units of LCMV Armstrong (WT LCMV; originally provided by Dr Michael Oldstone, The Scripps Research Institute) or a recombinant LCMV Armstrong strain (LCMV(ΔP14); a gift from Dr Dirk Homann, Icahn School of Medicine at Mount Sinai) in which the valine at position 35 of the LCMV glycoprotein is replaced by alanine thus precluding recognition by P14 or endogenous H2-D^b-GP_{33–41}-specific CD8 T cells as previously reported for an in vivo-selected LCMV variant⁴¹. LCMV(ΔP14) was originally generated by Dr Juan-Carlos de la Torre (The Scripps Research Institute, La Jolla) using an established plasmid-based viral rescue strategy^{54–56} and will be described elsewhere⁵⁷. Both LCMV strains were produced in BHK-21 cells (ATCC catalogue No. CCL-10) in DMEM with 2% FBS and infectious viral titres were assessed by plaque assays on Vero E6 (ATCC catalogue No. CRL-1586) monolayers.

Antibody treatments

For CD40L and MHC-II blocking experiments in vivo, mice were injected intravenously with 200 µg of CD40L-blocking antibody (clone MR-1, BioXCell) or subcutaneously with 150 µg of MHC-II (I-A and I-E) blocking antibody (clone M5/114, BioXCell), 4 h before the first injection of substrate.

Tamoxifen treatment

For induction of SrtA expression in T_{reg} cells and conventional T cells, *Foxp3*^{eGFP-CreERT2/Y}.*Rosa26*^{uLIPSTIC/WT} mice and CD4-CreERT2.*Rosa26*^{uLIPSTIC/WT} mice, respectively, were given two intragastric doses of 10 mg tamoxifen

Article

(Sigma-Aldrich) dissolved in corn oil (Sigma-Aldrich) at 4 and 2 days before the end point (day 0). For SrtA expression in germinal centre B cells, S1pr2-CreERT2.Rosa26^{uLIPSTIC/WT} mice and *Aicda*^{CreERT2/+}.Rosa26^{uLIPSTIC/WT} mice, two doses of 10 mg tamoxifen were administered intragastrically at 3 and 2 days before the end point. SrtA expression in gut epithelial cells was induced by daily injections (i.p.) of tamoxifen (2 mg per injection) for five consecutive days, starting 14 days before the end point. For SrtA expression in microglia of Cx3cr1^{CreER}.Rosa26^{uLIPSTIC/WT} mice, two doses of 10 mg of tamoxifen each were administered intragastrically at 6 and 4 days before the end point.

In vivo substrate administration

Biotin–aminohexanoic acid–LPETGS, carboxy-terminal amide, at 95% purity (biotin–LPTEG), was purchased from LifeTein (custom synthesis) and stock solutions were prepared in PBS at 20 mM. For *in vivo* LIPSTIC and uLIPSTIC labelling experiments in pLNs, biotin–LPETG was injected subcutaneously into the hind footpad (20 µl of 2.5 mM solution in PBS) six times 20 min apart, and pLNs were collected 20 min after the last injection, as described previously⁵⁸. Mice were briefly anaesthetized with isoflurane at each injection. For *in vivo* labelling of gut IELs, DCs and/or microglia in various tissues, and for LCMV experiments, biotin–LPETG substrate was injected i.p. (100 µl of 20 mM solution in PBS) six times, 20 min apart. Organs were collected 20 min after the last injection.

Isolation of lymphocytes from lymphoid organs

Spleen, pLNs, mLNs and mesenteric LN were collected into microfuge tubes with 500 µl HBSS (Gibco) supplemented with CaCl₂, MgCl₂ and collagenase D at 400 U ml⁻¹ (Roche). LN were cut into small pieces and incubated for 30 min at 37 °C. After digestion, tissue was forced five times through a 21-G needle and filtered through a 70-µm strainer into a 15-ml falcon tube with PBE.

Isolation of cells from non-lymphoid organs

Intraepithelial leukocytes were isolated as previously described⁵⁹. Briefly, small intestines were collected and washed in PBS. Peyer's patches were surgically removed and the intestine was segmented in pieces of approximately 1 cm before incubation with 1 mM dithiothreitol for 10 min at room temperature followed by addition of 30 mM EDTA and incubation for 30 min at 37 °C. Intraepithelial cells were recovered from the supernatant of dithiothreitol and EDTA washes and mononuclear cells were isolated by collecting the middle ring after 40% and 80% gradient Percoll centrifugation. Bone marrow cells were collected by centrifugation of punctured tibiae and femurs at up to 10,000g for 10 s, and then treated with ACK red blood cell lysing buffer. Immune cells from the kidney, lungs, spleen, thymus and liver were isolated by incubating the fragmented tissue in 1.5 ml HBSS supplemented with collagenase D at 400 U ml⁻¹, 0.1 mg ml⁻¹ DNase 1 (Sigma) and 0.8 mg ml⁻¹ dispase 1 (Sigma) for 30 min at 37 °C. After digestion, tissue was forced five times through a 21-G needle and filtered through a 70-µm strainer into a 15-ml falcon tube with PBE. Red blood cells were lysed with ACK buffer and the resulting cell suspensions were filtered through a 70-µm mesh into PBE. To collect immune cells from the brain, mice were anaesthetized and perfused transcardially with 10 ml ice-cold HBSS without Ca²⁺ and Mg²⁺ (HBSS–, Gibco), and the brains were removed and kept in ice-cold HBSS before further processing. To stain and discard CD45⁺ cells from blood vessels for downstream analysis, anti-CD45 antibodies were retro-orbitally injected 15 min before perfusion. The entire brain was minced by mashing through a 150-µm cell strainer and the strainer was washed thoroughly by ice-cold HBSS to collect as many cells as possible. Minced tissues were spun down at 290g for 5 min at 4 °C to discard the supernatant and digested in 2 ml of digestion solution (2 mg ml⁻¹ collagenase D, 25 mM HEPES, 1 mM sodium pyruvate, 14 µg ml⁻¹ DNase 1 in HBSS) for 20 min at 37 °C without shaking. Digestion was stopped by adding 2 ml ice-cold HBSS and the tissues were homogenized with syringes fitted with 21-G, 25-G and 27-G needles,

sequentially. The homogenates were filtered through a 70-µm mesh and spun down at 420g for 7 min at 4 °C to discard the supernatant. The pellets were resuspended in 37% Percoll solution in HBSS and centrifuged at 500g for 10 min at room temperature to discard supernatant with a myelin layer. The cells in pellets were washed and resuspended in HBSS for further analysis.

Flow cytometry and cell sorting

Single-cell suspensions were washed with PBE, incubated with 1 µg ml⁻¹ anti-CD16/32 (2.4G2, BioXCell) for 5 min at room temperature and then stained for cell surface markers at 4 °C for 20 min in PBS using the reagents listed in Supplementary Table 9. Cells were washed with PBE and stained with Zombie fixable viability dye (BioLegend) or fixable Aqua dead cell stain kit (Invitrogen) at room temperature for 15 min, and then washed with PBE and filtered through a 40-µm strainer for acquisition. For *in vivo* JAML staining of IELs, mice were injected i.p. with 100 µg of anti-JAML AF646 antibody 12 or 6 h before the end point. For single-cell transcriptomic analysis, stained cells were further incubated with DNA-barcoded anti-biotin and sample hashtag (anti-MHC-I) antibodies (BioLegend) for 20 min in PBE, washed three times with PBE and bulk-sorted. For substrate detection *in vivo*, an anti-biotin–PE antibody (Miltenyi Biotec) was exclusively used, as described previously⁵⁷. Samples were acquired on FACSymphony A5 or Fortessa analysers or sorted on FACSAria II or III or FACSymphony S6 cell sorters (BD Biosciences). Data were analysed using FlowJo v10.6.2 software.

uLIPSTIC labelling in vitro

HEK293T cells (ATCC) were transfected by calcium phosphate transfection with the indicated expression vectors at high (1 µg µl⁻¹) and low (0.1 µg µl⁻¹) concentrations of Thy1.1–G₅ and mSrtA constructs. Forty hours after transfection, cells were detached using TrypLE Express cell dissociation solution (Thermo Fisher), washed and resuspended at 10⁶ cells ml⁻¹ in PBS. Donor cell populations transfected with CD40L and/or mSrtA constructs and acceptor cell populations transfected with CD40 and/or Thy1.1–G₅ were mixed at a 1:1 ratio (10⁵ cells of each population) in a 1.5-ml conical tube, to which biotin–LPETG was added to a final concentration of 100 µM. Cells were incubated at room temperature for 30 min and washed three times with PBE to remove excess biotin–LPETG before FACS staining.

uLIPSTIC labelling ex vivo

B cells from Rosa26^{uLIPSTIC/WT} mice and CD4⁺ T cells from OT-II CD4-Cre.Rosa26^{uLIPSTIC/WT} mice were isolated from mouse spleens as described above. Isolated T cells were activated with CD3–CD28 Dynabeads (Thermo Fisher) for 24 h and then co-cultured with isolated B cells (2 × 10⁵ cells per well, 1:1 ratio) in the presence or absence of OVA^{323–339} peptide in RPMI, 10% FBS supplemented with 0.1% 2 mercaptoethanol (Gibco) in U-bottom 96-well plates for 20 h. Blocking antibodies were added at the beginning of the co-culture at a final concentration of 150 µg ml⁻¹. To label interactions *ex vivo*, biotin–LPETG substrate was added 30 min before collection at a final concentration of 100 µM.

Library preparation for scRNA-seq

In addition to fluorescent antibodies, cells were co-stained before sorting with hashtag oligonucleotide (HTO)-labelled antibodies to CD45 and MHC-I for sample separation (two hashtags per sample) and HTO–anti-biotin for detection of the uLIPSTIC signal. Sorted cells were collected into a microfuge tube with 300 µl PBS supplemented with 0.4% BSA. After the sort, tubes were topped with PBS 0.4% BSA and centrifuged, and the buffer was carefully reduced by removing the volume with a pipette to a final volume of 40 µl. Cells were counted for viability and immediately submitted to library preparation. The scRNA-seq library was prepared using the 10X Single Cell Chromium system, according to the manufacturer's instructions, at the Genomics Core of Rockefeller University and was sequenced on an Illumina

NovaSeq SP flowcell to a minimum sequencing depth of 30,000 reads per cell using read lengths of 26 bp read 1, 8 bp i7 index, 98 bp read 2.

Computational analysis of uLIPSTIC + scRNA-seq data in intraepithelial immune cells

Gene expression unique molecular identifier (UMI) counts, along with sample and biotin (uLIPSTIC) HTO counts, were generated with CellRanger v6.0.1 ‘count’ using ‘Feature Barcode’ counts and otherwise default parameters, with mm10 reference. TCR data were preprocessed with CellRanger ‘vdj’ with default parameters. Applying default cell-ranger filtering, this resulted in a filtered gene expression UMI count matrix including 4,607 cells and 32,285 genes.

We then carried out a multi-step analysis of the data to annotate cells with cell types, including data preprocessing, normalization, clustering and analysis of known marker genes from the literature as well as objective differential gene expression analysis. The scanpy package v1.9.1 was used for all analyses of the gene expression data⁶⁰. Cell barcodes with unresolved sample HTOs, a low or extremely high number of expressed genes, a large fraction of expressed mitochondrial genes, or those likely to represent doublets were removed. Genes expressed in a low number of cells were removed. This resulted in a filtered gene expression matrix of 3,677 cells and 14,332 genes with a matching biotin HTO count in each cell representing uLIPSTIC signal.

Gene counts were normalized using Pearson residual normalization with $\theta = 1$. Principal component analysis (PCA) was run with default parameters, and then a k -nearest neighbour (k NN) graph was constructed using 40 principal components (PCs), $k = 30$ and otherwise default parameters. Then Leiden clustering was carried out with a resolution of 1, resulting in 26 clusters. Cluster 10 was further split into two subclusters containing cycling T and B cells (Extended Data Fig. 6f,g).

uLIPSTIC normalized values were obtained for each cell by dividing the uLIPSTIC HTO counts by the number of sample-encoding HTO read counts in a cell. The fifth percentile of these normalized values was added as a pseudocount, and then \log_{10} was applied. These values were then shifted by the minimum log-scaled value, so the scale starts at 0. This resulted in arbitrary units of the normalized uLIPSTIC signal, subject to comparison between cells from a single dataset.

Known marker genes as well as TCR data were used to annotate the Leiden clusters. The sciripy package v0.10.1 was used for the TCR data preprocessing and analysis⁶¹. Cluster 10 was split into two subclusters that contained cycling T and B cells. Annotations were confirmed by scoring PanglaoDB immune cell marker gene sets⁶² using the score_genes() function in scanpy and by exploring significantly differentially expressed genes in each cluster as compared with all cells outside the cluster, obtained using a custom script. For differential expression analysis, $\log_2[\text{fold change}]$ ($\log_2[\text{FC}]$) of expression was calculated as the ratio of pseudobulk raw UMI counts summed over cells within and outside the cluster (then normalized by the total amount of UMI counts inside and outside the cluster). P values were calculated using the Mann–Whitney U-test applied to Pearson residual normalized expression values in single cells within and outside the cluster, and Benjamini–Hochberg correction for multiple hypothesis testing was applied to all genes. This analysis resulted in final cell type annotations; some clusters received the same cell type annotations.

The analysis then focused on the CD4 T cell subset of 944 cells. A new k NN graph was generated for this subset, again using $k = 30$ neighbours and 40 PCs, and Leiden clustering was carried out with resolution = 1.3. Clusters were annotated using known marker genes and TCR clonality information, and one cluster was filtered out owing to trouble annotating it, resulting in a dataset of 915 cells. Trajectory analysis and subsequent cell pseudotime calculation were carried out using Wishbone v0.5.2 (ref. 63) using default parameters as available in scanpy and using as the root the cell in the naive or T_{conv} cluster with the highest value of *Sell* expression. uLIPSTIC signal (normalized biotin) data were not used to generate the trajectory.

To identify candidate genes involved in cell–cell interactions, for every gene the Spearman correlation was calculated between the Pearson residual normalized value of expression of that gene and the uLIPSTIC signal across all cells in the CD4 T cell subset. Bonferroni correction was used for multiple hypothesis testing on all genes. This calculation was separately carried out when removing T_{FH} -like and naive or memory cells, or when restricting to cells from each individual mouse, with consistent results (Extended Data Fig. 8d,e).

For the violin plot of scRNA-seq expression of *Jam1* (Fig. 4i), Pearson residual normalized values were shifted so that the minimum value is zero (bottom fifth percentile of all values (across cell groups) omitted) and then plotted on a log scale. The T cell subpopulations for the plot were defined as follows. The subpopulations of CD4 T cells, ‘naive or T_{conv} ’, ‘pre-IEL’ and ‘IEL’ (Fig. 4d–h and Extended Data Fig. 8a,b), were used as $CD4^+ T_{\text{conv}}$, $CD4^+$ pre-IEL and $CD4^+ CD8\alpha\alpha^+$ IEL, respectively. The ‘natural IEL’ cells (Fig. 4b and Extended Data Figs. 6 and 7) were separated into three groups: $CD8\alpha\alpha^+$ IEL if TCR antibody chain was detected (301 cells), otherwise $\gamma\delta$ IEL if normalized expression of *Trdc* was above 0 (517 cells), and other (163 cells), which were not included in the plot.

MSigDB canonical pathways were scored using scanpy’s score_genes() function over all $CD4^+$ T cells. Spearman correlation with normalized biotin values was calculated for all pathways, and P values were adjusted using the q -value approach⁶⁴ for pathways with positive correlation values. The top five pathway scores are shown by correlation value, for those with $q < 0.05$ (Extended Data Fig. 8g). $CD4^+ CD103^+ CD8\alpha\alpha^+$ and $CD4^+ CD103^- CD8\alpha\alpha^-$ gene signatures were generated from scRNA-seq (library 2) from ref. 6. *tdTomato*[−] $CD4^+ CD8\alpha\alpha^+$ cells (cluster 2) were compared to *tdTomato*[−] ‘recent epithelial immigrants’ (REI, cluster 5) using the Wilcoxon rank sum test. P values were adjusted using Bonferroni correction. All genes with adjusted P values < 0.05 were included in the signature. Genes with positive fold change (enriched in cluster 2) were included in ‘ $CD4^+$ IEL, upregulated’ and those with negative fold change (enriched in cluster 5) were included in ‘ $CD4^+$ IEL, downregulated⁶. Signatures were scored on the uLIPSTIC scRNA-seq data using scanpy’s score_genes() function, and Spearman correlation with normalized biotin values for both gene signatures was calculated over all $CD4^+$ T cells, or over all $CD4^+$ T cells excluding T_{conv} and T_{FH} -like cells. The linear regression fit with the 95% confidence interval overlaid over the scatter plots was calculated using geom_smooth() in ggplot2 using default parameters.

Computational analysis of uLIPSTIC + scRNA-seq data in LCMV infection

Gene expression UMI counts, along with sample, biotin (uLIPSTIC) and Flag (to capture donor cells) HTO counts, were generated for each of the three sequencing lanes with CellRanger 7.0.1 ‘count’ using ‘Feature Barcode’ counts and otherwise default parameters, with mm10 reference. All downstream analysis was carried out using the scanpy package v1.9.1. Initial quality control steps and normalization were carried out separately for each of the three sequencing lanes. Cells were filtered on the basis of high mitochondrial counts and total counts. Genes were filtered on the basis of being present in at least 0.5% of cells in the sample, and cells were filtered to include at least 200 genes. Each cell was assigned to a sample if the fraction of all sample HTOs coming from that sample HTO was greater than 80%. For each cell, biotin read counts and donor (Flag) read counts were normalized by dividing by the total number of HTO counts of the sample to which the cell was assigned. Gene expression counts were then normalized with analytical Pearson residual normalization from scanpy, using a θ value of 1 for all three samples. After normalization, the three samples were concatenated. Non-protein-coding genes were also filtered out on the basis of the CellRanger mm10 GTF file. This resulted in a dataset of 27,043 cells and 11,558 genes.

LCMV LN cells from WT infection were selected for a separate analysis. This resulted in a dataset of 11,846 cells (and the same 11,558 genes). PCA was run with 100 components, a k NN graph was built using 30

Article

neighbours, 50 PCs and cosine metric, and Leiden clustering was carried out with a resolution of 1. Known marker genes were used to annotate the Leiden clusters.

As described above, sample-normalized biotin values were further adjusted by carrying out \log_{10} transformation, using the fifth percentile as a pseudocount, and then shifted by the minimum log-scaled value, so the scale starts at 0. Differential gene expression analysis was carried out as described above. Unless stated otherwise, in most plots, cells with high donor levels (using a threshold based on the distribution of these normalized Flag counts) were filtered out.

Next, LCMV organ cells (from spleen, liver and lung) in WT infection were selected for a separate analysis, yielding a dataset of 12,324 cells and 11,558 genes. PCA was run with 100 components, a k NN graph was built using 30 neighbours, 50 PCs and cosine metric, and Leiden clustering was carried out with a resolution of 1. To annotate these clusters and compare them to the LN data, a dendrogram of transcriptional similarities between cells in clusters was created. For this, we combined the mean profile for each tissue Leiden cluster and each cell type annotation in the LN data over all genes. This enabled us to find tissue Leiden clusters that have similar expression profiles as the LN annotations. Known marker gene expression was used to confirm these LN-based annotations in the tissue data. Certain clusters did not relate to LN annotations, so most significant differentially expressed genes (following the same protocol as described above) for these clusters were used to assign annotations with the ImmGen My_Geneset tool (<https://www.immgen.org>). These annotations were again confirmed with marker gene expression.

As described above, biotin read counts and donor (Flag) read counts were normalized by dividing by the total number of HTO counts of the sample to which the cell was assigned. The sample-normalized biotin values were further adjusted by carrying out \log_{10} transformation, using the fifth percentile as a pseudocount, and then shifted by the minimum log-scaled value, so the scale starts at 0. For most plots, cells with high donor levels (using a threshold based on the distribution of the sample-normalized Flag counts) were filtered out.

Modelling the SrtA-Thy1.1 complex on cells surfaces

First, structures of G₅-Thy1.1 and Flag-SrtA-PDGFRb were generated using AlphaFold2 (ref. 65). Next, in the Flag-SrtA-PDGFRB model, the domain constructing peptide-binding-domain was substituted with the substrate-bound SrtA structure (Protein Data Bank: 1T2W). Additionally, the flexible linker connecting the SrtA domain to the PDGFRB transmembrane helix was rebuilt to an extended conformation using COOT v. 0.8.9.2 (ref. 66) to better estimate the maximum distance the protein is able to extend to. The Thy1.1 was aligned to SrtA using the substrate of 1T2W and the 5G acceptor motif of G₅-Thy1.1. Any resulting interprotein clashes were corrected using GalaxyRefineComplex from the GalaxyWEB server (<https://galaxy.seoklab.org/>)⁶⁷. To build the GPI anchor and the lipid bilayers, we used CHARMM-GUI (<https://www.charmm-gui.org/>)⁶⁸. The anchor glycolipid was generated on the basis of the human prion protein (PrP) GPI⁶⁹. Next the complex of Flag-SrtA-PDGFRB with G₅-Thy1.1 was modelled in the POPC-cholesterol lipid bilayer using CHARMM-GUI. The GPI anchor was placed in the second bilayer using ChimeraX v1.4 (ref. 70). Finally, both modelled bilayers, one embedded with the protein complex and the other with the GPI anchor, were aligned in ChimeraX. The distance between two bilayers was measured in PyMOL v2.4.2 (ref. 71).

Statistical analysis

Statistical tests were carried out in GraphPad Prism 9.0 software and edited for appearance using Adobe Illustrator 27.1.1. Comparisons between two treatment conditions were analysed using unpaired, two-tailed Student's *t*-test and multivariate data were analysed by one-way analysis of variance with Tukey's post-hoc tests to further examine pairwise differences.

Reporting summary

Further information on research design is available in the Nature Portfolio Reporting Summary linked to this article.

Data availability

Final scRNA-seq datasets are available from the Gene Expression Omnibus under the accession number GSE253000. Processed scRNA-seq data are available at <https://github.com/pritykinlab/ulipstic-analysis>. Source data are provided with this paper.

Code availability

The full code used to analyse the scRNA-seq data is available at <https://github.com/pritykinlab/ulipstic-analysis>.

46. Engels, B. et al. Retroviral vectors for high-level transgene expression in T lymphocytes. *Hum. Gene Ther.* **14**, 1155–1168 (2003).
47. Kim, J. H. et al. High cleavage efficiency of a 2A peptide derived from porcine teschovirus-1 in human cell lines, zebrafish and mice. *PLoS ONE* **6**, e18556 (2011).
48. Argos, P. An investigation of oligopeptides linking domains in protein tertiary structures and possible candidates for general gene fusion. *J. Mol. Biol.* **211**, 943–958 (1990).
49. Lee, P. P. et al. A critical role for Dnmt1 and DNA methylation in T cell development, function, and survival. *Immunity* **15**, 763–774 (2001).
50. Schraml, B. U. et al. Genetic tracing via DNGR-1 expression history defines dendritic cells as a hematopoietic lineage. *Cell* **154**, 843–858 (2013).
51. Shinmatsu, R. et al. Regulated selection of germinal-center cells into the memory B cell compartment. *Nat. Immunol.* **17**, 861–869 (2016).
52. Barnden, M. J., Allison, J., Heath, W. R. & Carbone, F. R. Defective TCR expression in transgenic mice constructed using cDNA-based alpha- and beta-chain genes under the control of heterologous regulatory elements. *Immunol. Cell Biol.* **76**, 34–40 (1998).
53. Danciu, C. et al. A characterization of four B16 murine melanoma cell sublines molecular fingerprint and proliferation behavior. *Cancer Cell Int.* **13**, 75 (2013).
54. Sanchez, A. B. & de la Torre, J. C. Rescue of the prototypic Arenavirus LCMV entirely from plasmid. *Virology* **350**, 370–380 (2006).
55. Emonet, S. F., Garidou, L., McGavern, D. B. & de la Torre, J. C. Generation of recombinant lymphocytic choriomeningitis viruses with trisegmented genomes stably expressing two additional genes of interest. *Proc. Natl Acad. Sci. USA* **106**, 3473–3478 (2009).
56. Iwasaki, M., Ngo, N., Cubitt, B., Teijaro, J. R. & de la Torre, J. C. General molecular strategy for development of arenavirus live-attenuated vaccines. *J. Virol.* **89**, 12166–12177 (2015).
57. van der Heide, V. et al. Functional impairment of “helpless” CD8+ memory T cells is transient and driven by prolonged but finite cognate antigen presentation. Preprint at [bioRxiv https://doi.org/10.1101/2024.01.22.576725](https://doi.org/10.1101/2024.01.22.576725) (2024).
58. Pasqual, G., Angelini, A. & Victora, G. D. Triggering positive selection of germinal center B cells by antigen targeting to DEC-205. *Methods Mol. Biol.* **1291**, 125–134 (2015).
59. Bilate, A. M. et al. Tissue-specific emergence of regulatory and intraepithelial T cells from a clonal T cell precursor. *Sci. Immunol.* **1**, eaaf7471 (2016).
60. Wolf, F. A., Angerer, P. & Theis, F. J. SCANPY: large-scale single-cell gene expression data analysis. *Genome Biol.* **19**, 15 (2018).
61. Sturm, G. et al. Scirpy: a Scanpy extension for analyzing single-cell T-cell receptor sequencing data. *Bioinformatics* **36**, 4817–4818 (2020).
62. Franzén, O., Gan, L. M. & Björkegren, J. L. M. PanglaDB: a web server for exploration of mouse and human single-cell RNA sequencing data. *Database* **2019**, baz046 (2019).
63. Setty, M. et al. Wishbone identifies bifurcating developmental trajectories from single-cell data. *Nat. Biotechnol.* **34**, 637–645 (2016).
64. Storey, J. D. & Tibshirani, R. Statistical significance for genomewide studies. *Proc. Natl Acad. Sci. USA* **100**, 9440–9445 (2003).
65. Jumper, J. et al. Highly accurate protein structure prediction with AlphaFold. *Nature* **596**, 583–589 (2021).
66. Emsley, P. & Cowtan, K. Coot: model-building tools for molecular graphics. *Acta Crystallogr. D* **60**, 2126–2132 (2004).
67. Ko, J., Park, H., Heo, L. & Seok, C. GalaxyWEB server for protein structure prediction and refinement. *Nucleic Acids Res.* **40**, W294–W297 (2012).
68. Jo, S., Kim, T., Iyer, V. G. & Im, W. CHARMM-GUI: a web-based graphical user interface for CHARMM. *J. Comput. Chem.* **29**, 1859–1865 (2008).
69. Paulick, M. G. & Bertozzi, C. R. The glycosylphosphatidylinositol anchor: a complex membrane-anchoring structure for proteins. *Biochemistry* **47**, 6991–7000 (2008).
70. Goddard, T. D. et al. UCSF ChimeraX: meeting modern challenges in visualization and analysis. *Protein Sci.* **27**, 14–25 (2018).
71. PyMOL v2.4.0 (Schrödinger & DeLano, 2020).
72. Butler, A., Hoffman, P., Smibert, P., Papalexi, E. & Satija, R. Integrating single-cell transcriptomic data across different conditions, technologies, and species. *Nat. Biotechnol.* **36**, 411–420 (2018).

Acknowledgements We thank the Rockefeller University Transgenics and Gene Targeting facilities for generating the uLIPSTIC mouse strain; the Comparative Biosciences Center for mouse housing; T. B. R. Castro for bioinformatics assistance; C. L. Ferreira for mouse genotyping; K. Gordon and J.-P. Truman for cell sorting; all Rockefeller University staff for their continuous support; C. Reise Sousa, T. Kuroasaki, T. Okada, C.-A. Reynaud and Jean-Claude Weill

for mice; J. Merkenschlager for altered peptide ligands; and T. Catarino and H. Veiga-Fernandes for preliminary contributions to the development of the uLIPSTIC system. This study was supported by the National Institutes of Health (NIH) grants DP1AI144248 (Pioneer award) and R01AI173086 to G.D.V., DP2AI171161 to Y.P., R01AR050452 and R01AR27883 to E.F., R01AI153363 to A.O.K. and V.v.d.H., and Starr Consortium grant I10-0044 to G.D.V. Work in the laboratory of G.D.V. is additionally supported by the Robertson Foundation, and work in the laboratory of Y.P. is additionally supported by the Ludwig Institute for Cancer Research. S.N.-H. was supported by a Bulgari Women & Science Fellowship. S.W. was supported by the NIH National Human Genome Research Institute training grant 5T32HG003284, M.C.C.C. was supported by the Pew Latin American Fellows Program, A.C. was supported by a Damon Runyon Postdoctoral Fellowship, and S.M.P. was supported by a Cancer Research Institute Carson Family Postdoctoral Fellowship (CRI4498). E.F. and D.M. are HHMI investigators. G.D.V. is a Burroughs Wellcome Investigator in the Pathogenesis of Infectious Disease and a Pew-Stewart Scholar.

Author contributions S.N.-H. carried out all experimental work with assistance from M.C.C.C., A.C., J.T.J., J.B. and S.M.P. S.W. and Y.P. designed and carried out all computational analyses. V.v.d.H. and A.O.K. contributed to the design, performance and interpretation of LCMV

experiments. K.F. generated the structural model of the interaction between SrtA and G_s-Thy1.1. G.P. conceived the uLIPSTIC system along with G.D.V., Y.P., A.M.B., E.F., D.M. and G.D.V. supervised the work. S.N.-H., S.W., Y.P. and G.D.V. wrote the manuscript, with input from all authors.

Competing interests G.D.V. is an adviser for and owns stock futures in the Vaccine Company, Inc. E.F. recently served on the scientific advisory boards of L'Oréal and Arsenal Biosciences and owns stock futures in the latter company.

Additional information

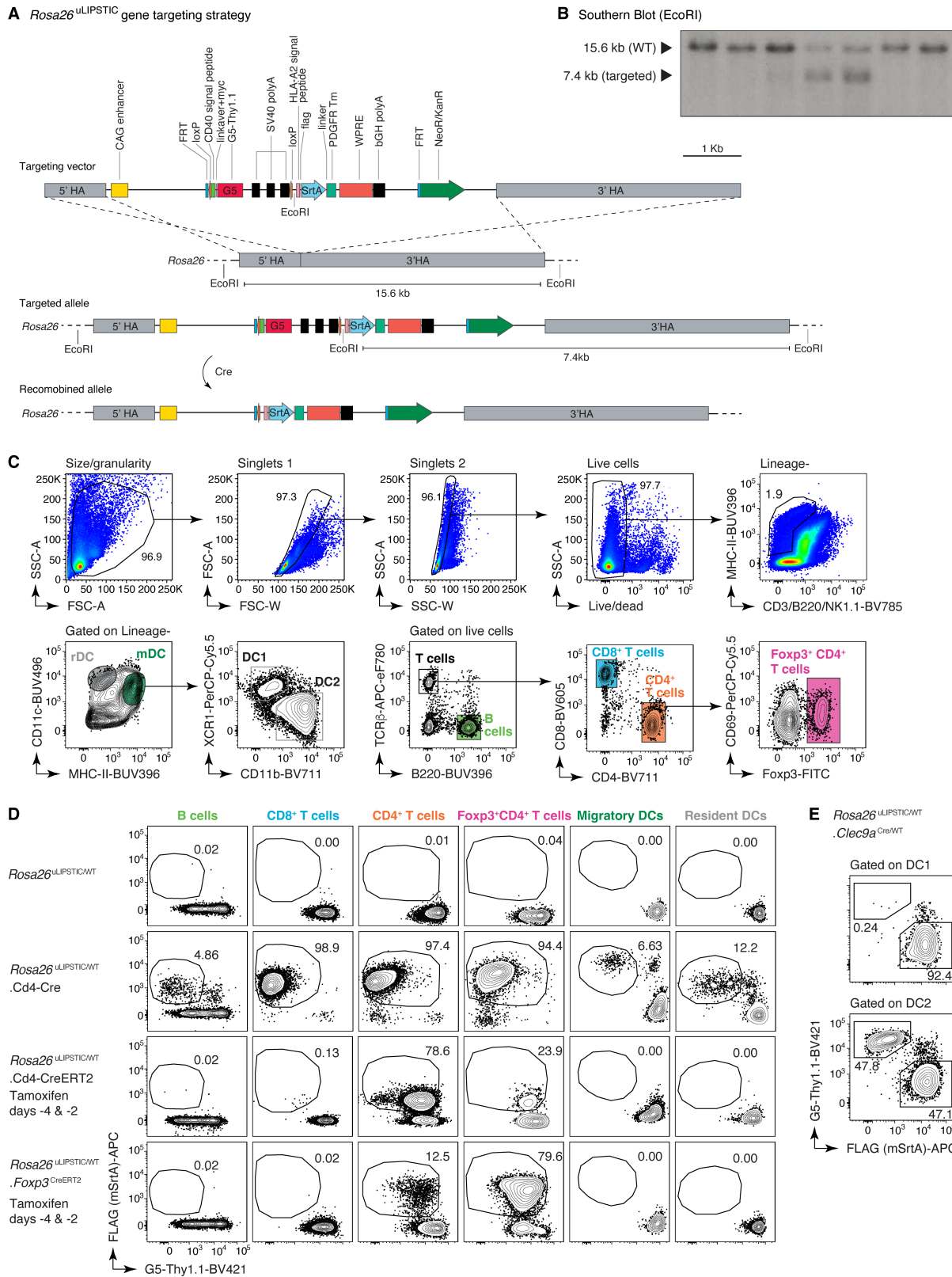
Supplementary information The online version contains supplementary material available at <https://doi.org/10.1038/s41586-024-07134-4>.

Correspondence and requests for materials should be addressed to Yuri Pritykin or Gabriel D. Victora.

Peer review information *Nature* thanks Thorsten Mempel and the other, anonymous, reviewer(s) for their contribution to the peer review of this work.

Reprints and permissions information is available at <http://www.nature.com/reprints>.

Article



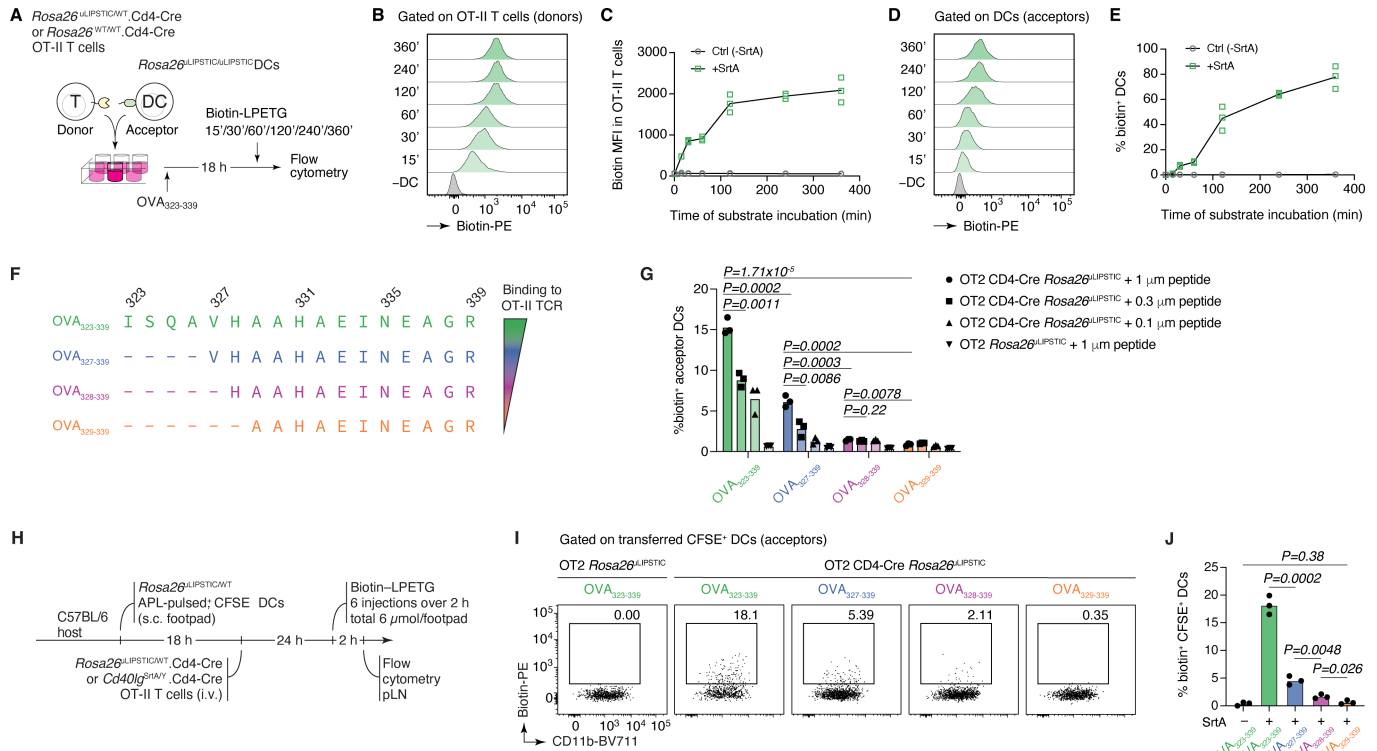
Extended Data Fig. 1 | See next page for caption.

Extended Data Fig. 1 | Design and characterization of *Rosa26*^{uLIPSTIC} mice.

(A) The uLIPSTIC cassette carrying the lox-stop-lox G_sThy1.1 followed by mSrtA-PDGFRtm fused to FLAG tag was cloned into the Ai9 *Rosa26* targeting plasmid. (B) Insertion of the uLIPSTIC cassette was assessed in embryonic stem (ES) cells by Southern blotting using a ³²P-labeled probe (Supplementary Table 8 and Supplementary Fig. 1 for gel source data) annealing upstream of the left arm after EcoRI digestion. ESCs carrying the insertion exhibit an extra EcoRI restriction site, resulting in a 7.4 kb fragment upon enzymatic digestion. The blot shows 2 heterozygous integrations out of 7 ES cell clones screened. (C–E) The specificity and efficiency of *Rosa26*^{uLIPSTIC} recombination are determined by the Cre driver used. (C) Representative gating strategy for

resident dendritic cells (rDCs; LIN⁻, MHC-II^{int}, CD11c^{hi}), migratory dendritic cells (mDCs; LIN⁻, MHC-II^{hi}, CD11c⁺), CD4⁺ T cells, CD8⁺ T cells, regulatory T (Treg) cells and B cells in lymph nodes. (D) SrtA expression (determined by FLAG detection) is induced by Cre recombination. Use of a constitutive Cre line (e.g., CD4-Cre) results in efficient but non-specific SrtA expression, generating T cells that can only be used in adoptive cell transfer experiments. The use of inducible Cre lines such as CD4-CreERT2 and *Foxp3*^{CreERT2} can often resolve specificity issues, enabling the implementation of uLIPSTIC in fully endogenous models. (E) SrtA expression in conventional DC subsets 1 (cDC1) and 2 (cDC2) in *Rosa26*^{uLIPSTIC/WT}.*Clec9a*^{Cre/WT} mice.

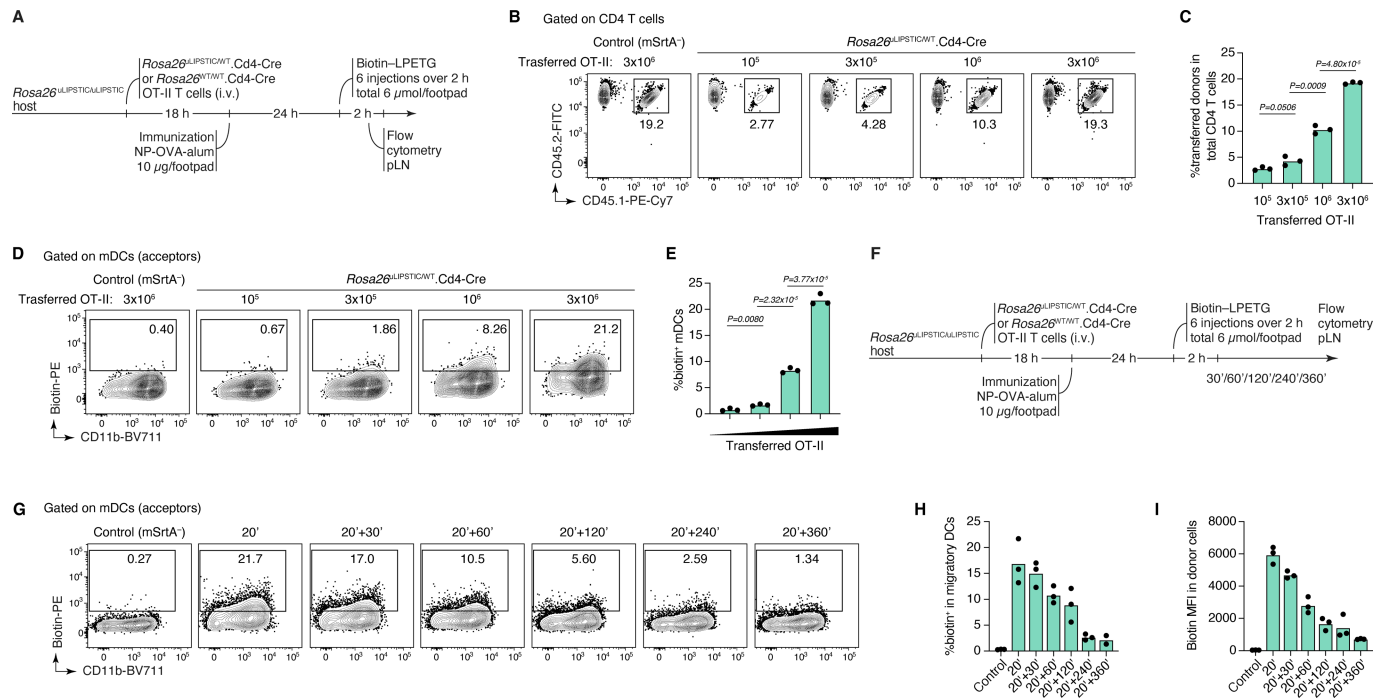
Article



Extended Data Fig. 2 | Kinetics and sensitivity of the uLIPSTIC reaction.

(A–E) Kinetics of the uLIPSTIC reaction. (A) Experimental setup for panels (B–E). OT-II CD4⁺ T cells from Rosa $26^{\text{uLIPSTIC}/\text{WT}}$.CD4-Cre or Rosa $26^{\text{WT}/\text{WT}}$.CD4-Cre control mice were co-incubated ex vivo with Rosa $26^{\text{uLIPSTIC}/\text{uLIPSTIC}}$ acceptor DCs in the presence of OVA $_{323-339}$ cognate peptide. LIPSTIC substrate was added during the final minutes of incubation as indicated. (B,C) Efficiency of formation of the acyl intermediate (loading of LIPSTIC substrate onto SrtA) in OT-II SrtA⁺ donor T cells increases gradually with time. (D,E) Transfer of LIPSTIC substrate onto the surface of interacting acceptor DCs followed similar kinetics as acyl intermediate formation. (F–J) uLIPSTIC can resolve differences in peptide

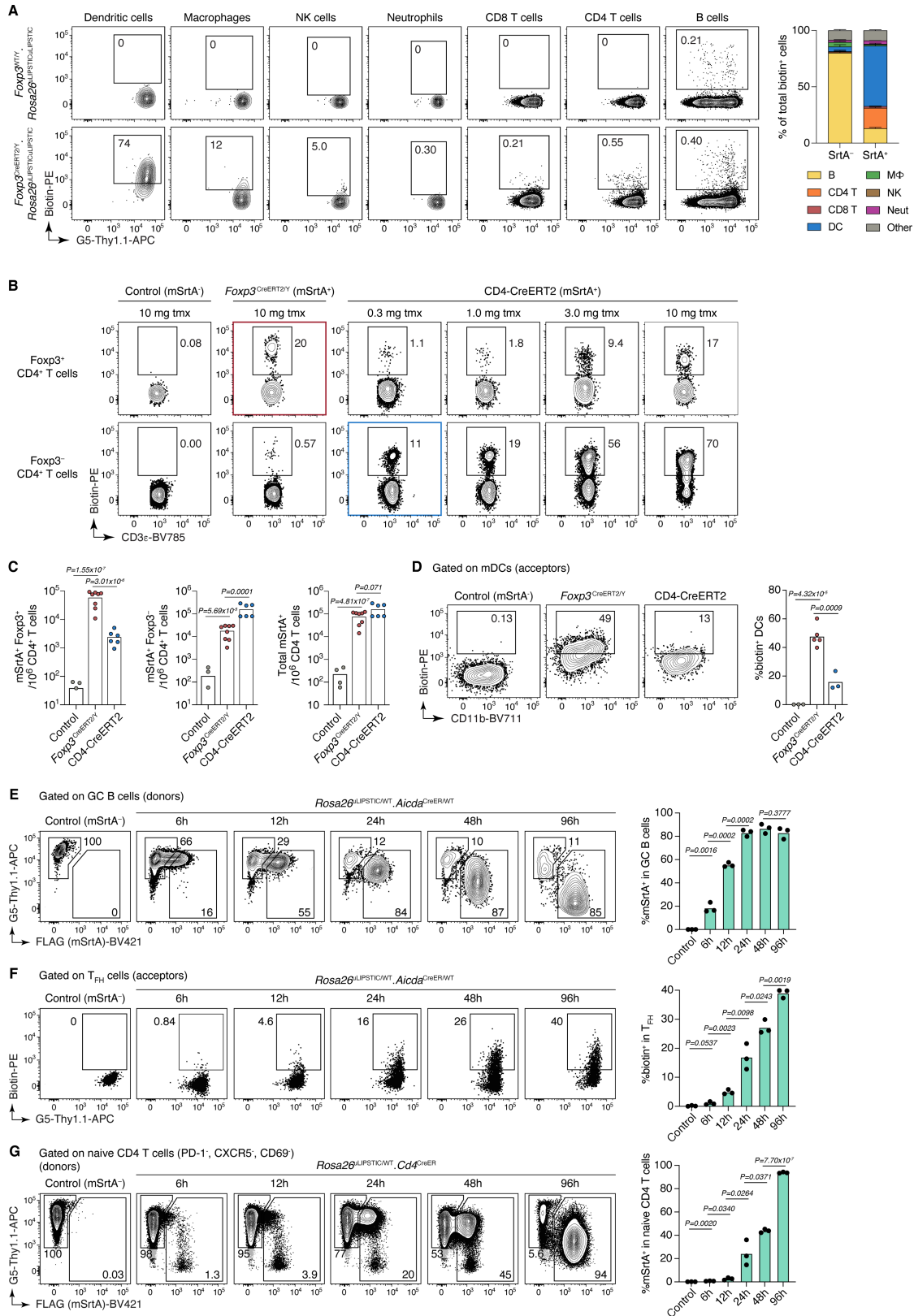
concentration and affinity both in vitro and in vivo. (F) Altered peptide ligands (APLs) of the OVA $_{323-339}$ peptide, when complexed with MHC-II, display decreasing affinities for the OT-II TCR. (G) In vitro co-culture of Rosa $26^{\text{uLIPSTIC}/\text{WT}}$.CD4-Cre OT-II T cells with Rosa $26^{\text{uLIPSTIC}/\text{uLIPSTIC}}$ DCs loaded with its APLs results in a reduction in LIPSTIC labeling that aligns with both the affinity of the peptide-MHCII complex to the OT-II TCR and the peptide concentration gradients. (H) Experimental layout for panels (I,J). (I) In vivo labeling of APL-pulsed DCs show decreased uLIPSTIC labeling in accordance with the affinity to the fixed OT-II TCR. Quantified in (J). Data for all plots are for three mice per condition from one experiment. P-values were calculated using two-tailed Student's tests.



Extended Data Fig. 3 | uLIPSTIC labeling of T cell–DC interactions in adaptive transfer models. (A–E) mSrtA⁺ donor cell numbers determine the degree of uLIPSTIC labeling. (A) Experimental layout for panels (B–E). Increasing numbers (10^5 , 3×10^5 , 10^6 , 3×10^6) of Rosa²⁶^{uLIPSTIC/+}.Cd4-Cre OT-II CD4⁺ T cells were adoptively transferred into recipient Rosa²⁶^{uLIPSTIC/uLIPSTIC} mice, followed by OVA/alum immunization 18 h post-transfer and LIPSTIC substrate injection one day later. The number of transferred cells (CD45.1/2)

determined the proportion of donor cells in the CD4⁺ T cell compartment (B–C) and the corresponding percentage of labeled interacting cells in the mDC compartment (D–E). (F–I) Persistence of label on acceptor cells with time. (F) Experimental layout for panels (G–I). (G) uLIPSTIC labeling of mDCs after incremental delays between substrate injection and tissue harvest. Quantified in (H,I). Data for all plots are for three mice per condition from one experiment. P-values were calculated using two-tailed Student's tests.

Article



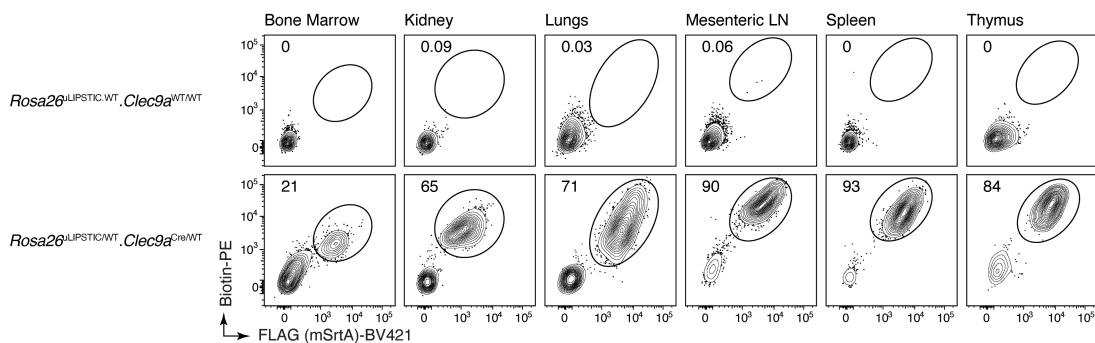
Extended Data Fig. 4 | See next page for caption.

Extended Data Fig. 4 | uLIPSTIC labeling in inducible Cre lines in fully endogenous models. (A–D) uLIPSTIC labeling of Treg cell interactions in the steady-state pLN. (A) Cellular interactome of Tregs at steady-state. *Rosa26*^{uLIPSTIC/WT}.*Foxp3*^{CreERT2/Y} experimental mice and *Rosa26*^{WT/WT}.*Foxp3*^{CreERT2/Y} controls were given tamoxifen and administered LIPSTIC substrate in the footpad 2 days later. *Left*, flow cytometry plots show uLIPSTIC labeling in selected immune populations in control (*top*) and experimental (*bottom*) mice. The presence of residual labeling in B cells is an artifact common to uLIPSTIC and to other flow-cytometry based methods aimed at identifying rare B cell populations, likely due to B cell receptor-dependent binding of detection components by polyclonal B cells. *Right*, quantification of the proportion of all labeled cells belonging to each major immune population in control (SrtA⁺) or experimental (SrtA⁺) mice. Data for three mice per condition from one experiment, bar plots show mean ± SEM. (B–D) Treg cells interact with mDCs to a greater extent than conventional CD4⁺ T cells. (B) To test if enhanced interaction with mDCs is a specific feature of Treg cells or a general feature of all CD4⁺ T cells, we titrated the dose of tamoxifen in *Rosa26*^{uLIPSTIC/+}.CD4-CreERT2 mice to achieve a similar percentage of SrtA-expression among total CD4⁺ T cells as in *Rosa26*^{uLIPSTIC/+}.*Foxp3*^{CreERT2/Y} mice. (C) At a dose of 0.3 mg of tamoxifen, *Rosa26*^{uLIPSTIC/+}.CD4-CreERT2 mice showed SrtA expression in a

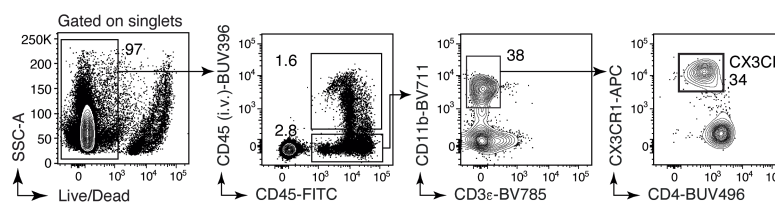
small number of Treg cells (*left*), with most SrtA⁺ cells observed in CD4⁺ conventional T cells (*center*) and overall numbers of SrtA⁺ cells among total CD4⁺ T cells that were comparable with those of *Rosa26*^{uLIPSTIC/+}.*Foxp3*^{CreERT2/Y} mice treated with 10 mg tamoxifen (*right*). (D) When numbers of Treg and CD4⁺ conventional donor cells are equalized, acceptor mDCs show stronger interaction with Treg cell partners. For (C) and (D), data from two independent experiments with each symbol representing one mouse, P-values were calculated using two-tailed Student's tests. (E–G) Kinetics of tamoxifen-driven recombination of the *Rosa26*^{uLIPSTIC} allele according to cell type. (E) SrtA expression in the highly proliferative mesenteric lymph node GC B cells of *Rosa26*^{uLIPSTIC/WT}.*Aicda*^{CreER/WT} mice was assessed at different timepoints after tamoxifen administration. The fraction of recombined cells plateaus at 24 h post-tamoxifen administration (hpt), while SrtA protein expression is still increasing by 96 hpt. (F) Labeling of GC B cell interacting partners can be detected as early as 12 hpt, increasing thereafter according to SrtA expression levels. (G) In contrast, SrtA expression in quiescent naïve (PD-1⁺CXCR5⁺CD69[−]) CD4⁺ T cells in *Rosa26*^{uLIPSTIC/WT}.Cd4-CreERT2 mice increased at a slower rate than, reaching >80% positive cells only at 96 hpt. For (E), (F) and (G), each plot used three mice per condition from one experiment, P-values were calculated using two-tailed Student's tests.

Article

A Gated on DCs: Lineage(NK1.1,B220,CD3)⁻, MHC-II^{hi}, CD11c⁺

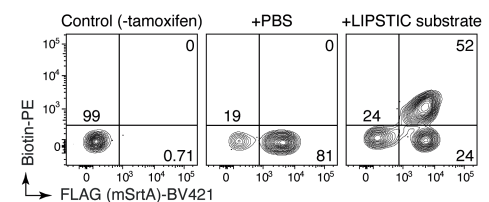


B Brain parenchyma

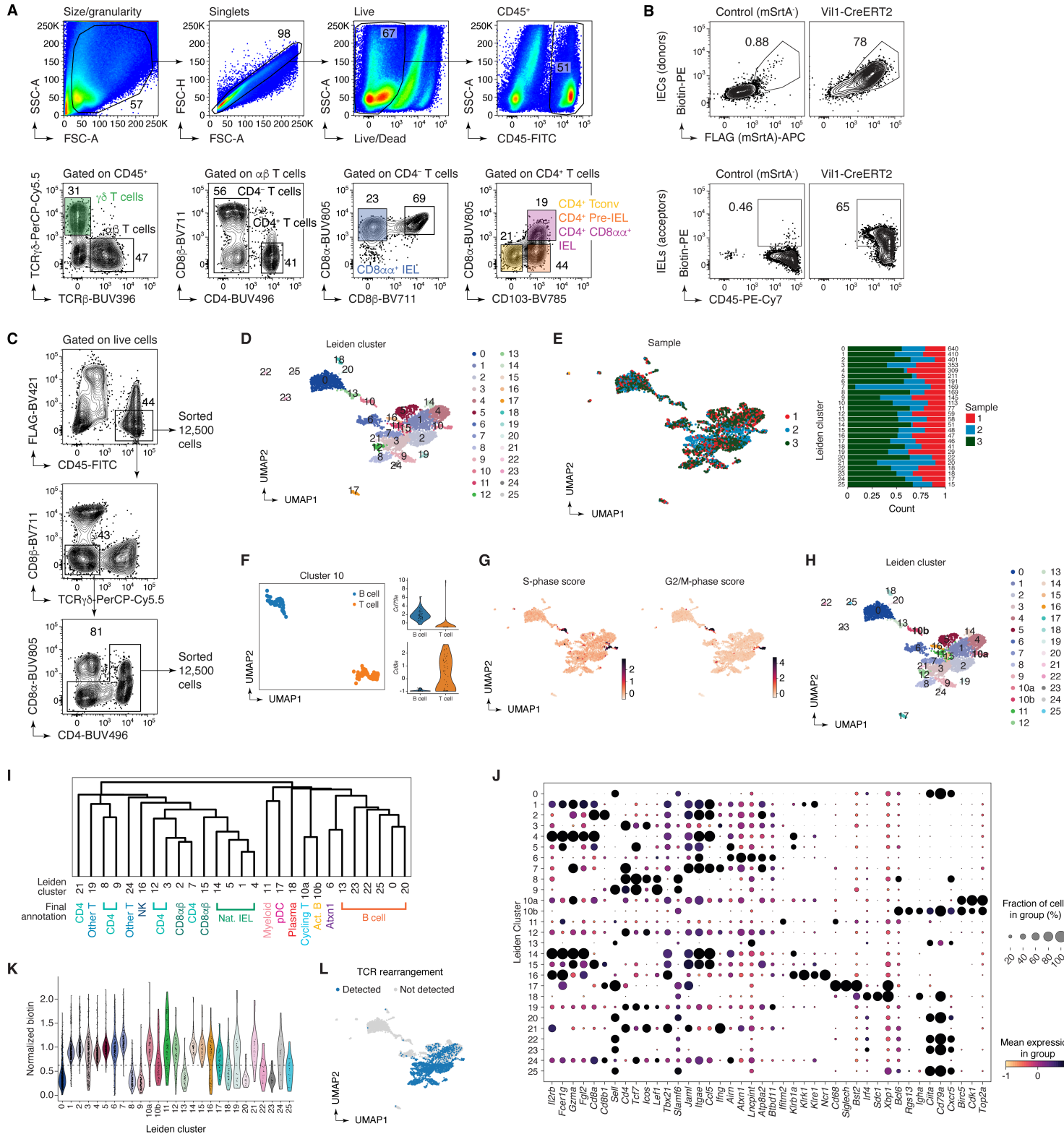


Extended Data Fig. 5 | Intraperitoneally-injected LIPSTIC substrate reaches cells in multiple tissues. (A) Steady state *Rosa26*^{LIPSTIC/WT}, *Clec9a*^{CreER/WT} or *Rosa26*^{LIPSTIC/WT}, *Clec9a*^{WT/WT} control mice were injected i.p. with the LIPSTIC substrate and its loading onto DCs was achieved in all analyzed tissues. (B-C) I.p. injection of the LIPSTIC substrate reaches the brain in *Rosa26*^{LIPSTIC/WT}, *Cx3cr1*^{CreERT2/WT} mice.

C *Rosa26*^{LIPSTIC/WT}, *Cx3cr1*^{CreERT2/WT}: Gated on CD11b⁺ CX3CR1⁺



mice. (B) Flow cytometry gating strategy to analyze CX3CR1-expressing microglia in the brain. To discriminate resident from circulating immune cells in the brain, α -CD45 antibody was injected intravenously to mark the latter. (C) SrtA expression was detected in ~80% of CD11b⁺CX3CR1⁺ cells, 68% of which acquired i.p.-administered LIPSTIC substrate.

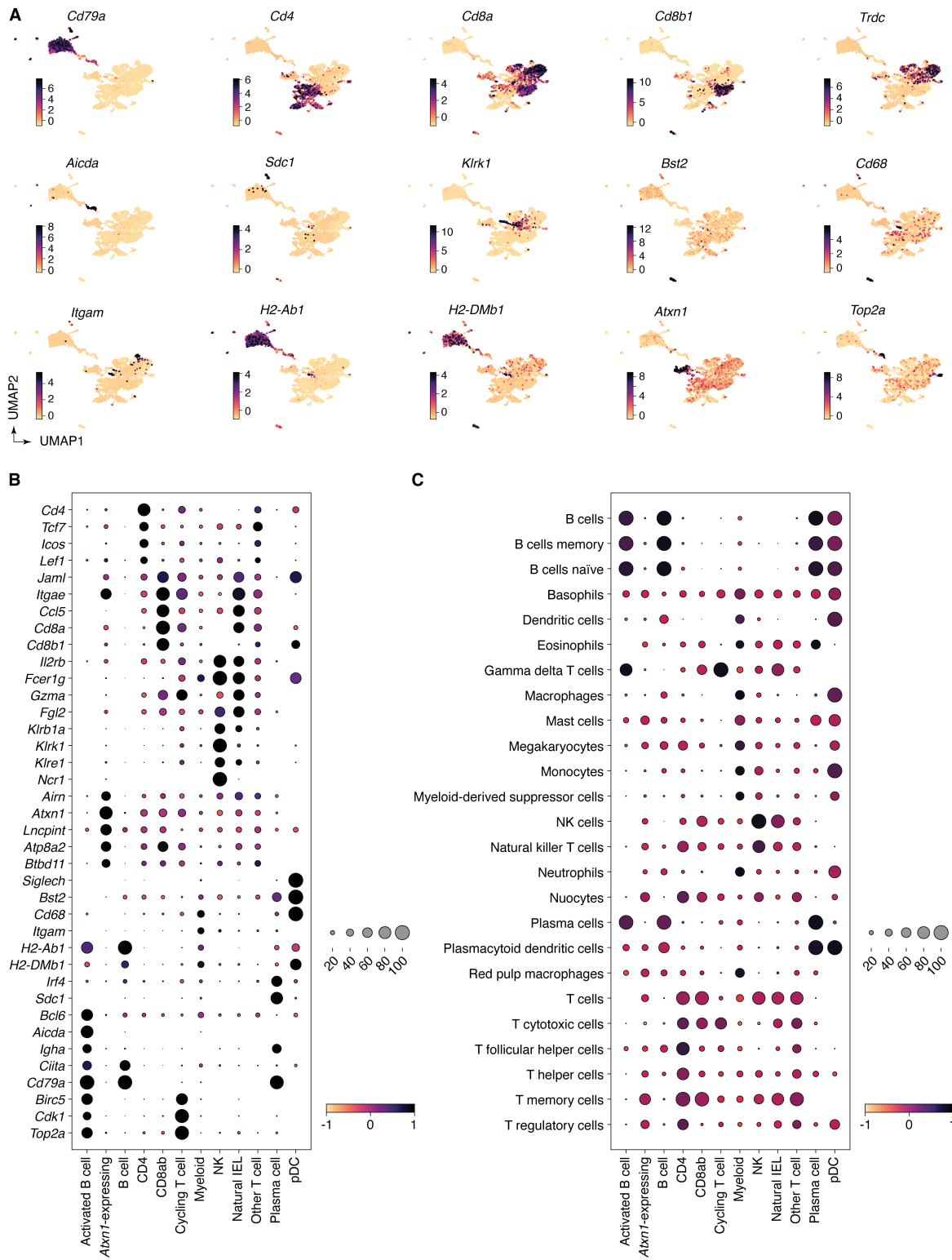


Extended Data Fig. 6 | See next page for caption.

Article

Extended Data Fig. 6 | uLIPSTIC to study epithelial cell – immune cell interactions in the gut. (A–C) Flow cytometry strategy for intraepithelial immune cells. (A) Representative gating strategy for $\gamma\delta$ TCR and $\alpha\beta$ TCR ($CD8\alpha\alpha^+$, $CD8\alpha\beta^+$, and $CD4^+$) IEL subsets. (B) *Top*, expression of SrtA (FLAG) and capture of LIPSTIC substrate by IEC donor cells and *bottom*, transfer of substrate onto $CD45^+$ acceptor cells in SrtA-expressing and control mice. (C) Sorting strategy for the scRNA-seq experiment. Samples were enriched for rarer (e.g., B cell, $CD4^+$ IEL) populations by first sorting 12,500 total cells then an additional 12,500 cells depleted of the dominant $\gamma\delta$, $CD8\alpha\alpha$, and $CD8\alpha\beta$ IEL populations. Three independent samples were sorted and stained with different hashtag oligos for downstream identification. (D–L) Clustering analysis of the immune interactome of IECs in the small intestine. (D) UMAP colored by Leiden clustering of the entire scRNA-seq-uLIPSTIC dataset ($n = 3,677$ cells) used as an intermediate step in cell type annotations. (E) *Left*, UMAP colored by biological replicate. *Right*, bar plot indicating cluster composition by biological replicate, cluster size indicated at the right of each bar. (F–G) Further analysis of cluster 10 shows that is a composite comprising proliferating T and B cells. This co-clustering of B and T cells held true for varying number of PCs between 20 and 100 (not shown). (F) *Left*, Leiden cluster

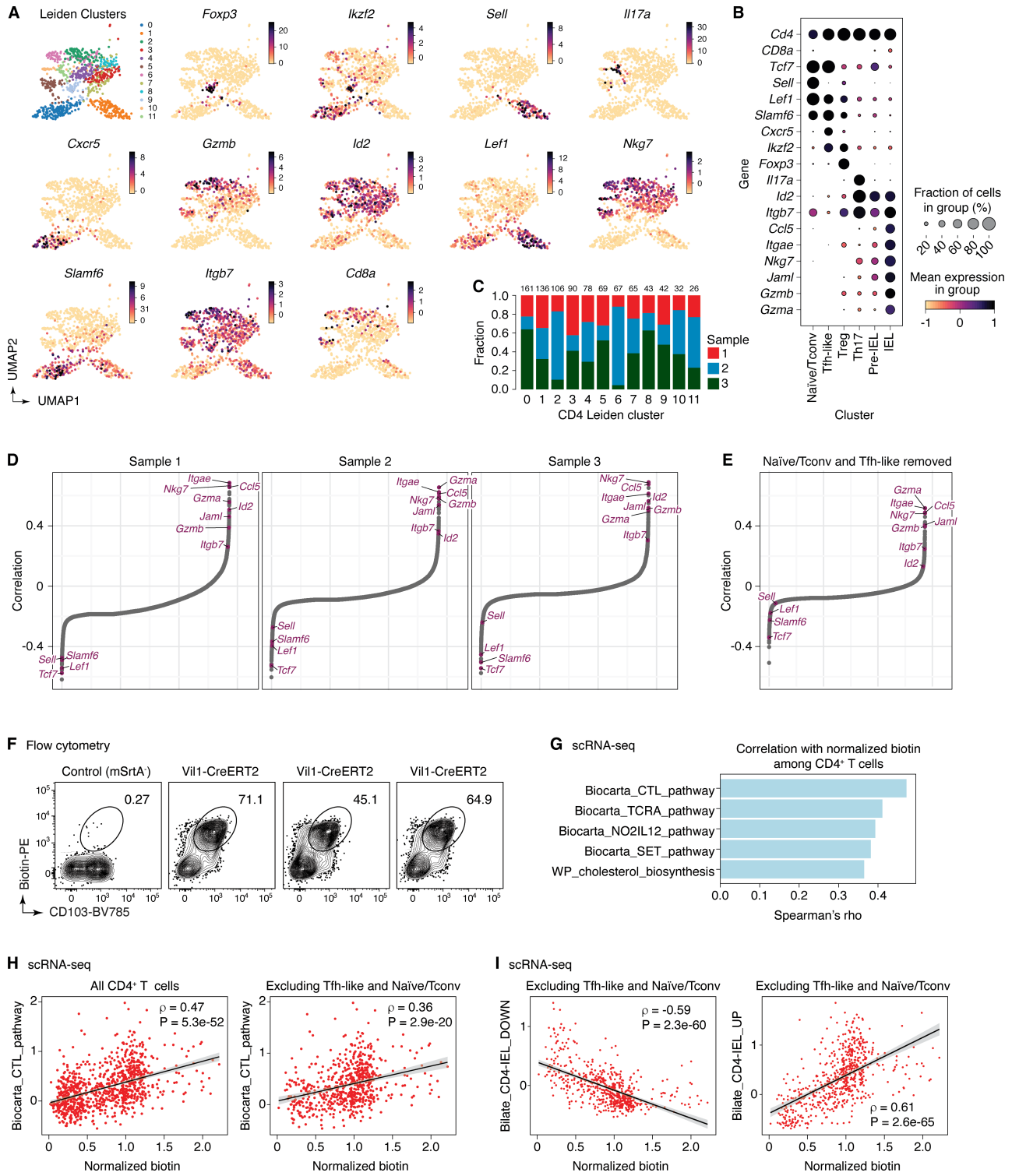
10 was isolated and sub-clustered, yielding two separate clusters (UMAP). *Right*, normalized expression of $Cd79a$ and $Cd8a$ for these two sub-clusters of cluster 10 determines their annotation as either B or T cells. (G) UMAP showing the S and G2M phase cell cycle gene list scores (obtained using the ‘score_genes_cell_cycle()’ function with lists from the Seurat package⁷²), characterizing Leiden cluster 10 as proliferating cells, thus explaining their co-clustering. (H) UMAP showing final clustering of the entire data, with Leiden cluster 10 subdivided into clusters 10a and 10b. (I) Dendrogram representing transcriptional similarities among clusters. Differentially expressed genes were identified for each cluster ($\log_{2}FC > 1$, $FDR < 0.05$, see Methods), and normalized expression of all such genes (5,956 genes total), averaged per cluster, was used for the hierarchical clustering analysis that produced the dendrogram. Final annotation clusters shown in Fig. 4 are indicated below the Leiden cluster numbers. (J) Dot plot of marker genes indicating their level of expression in each cluster. Dot size indicates the fraction of cells in the cluster with Pearson residual normalized expression greater than 0, dot color represents level of expression. (K) Violin plot showing levels of normalized uLIPSTIC signal for each Leiden cluster. (L) UMAP showing presence of rearranged TCR α and β in each cell.



Extended Data Fig. 7 | Expression of marker genes and gene signatures in the annotated scRNA-seq data. (A) UMAP plots showing normalized gene expression levels for selected marker genes characteristic of the final annotation clus. (B) Dot plot of marker genes indicating level of expression for each cell type annotation. (C) Dot plot of scores for gene signatures of immune

cell types from PanglaoDB⁶². For both dot plots, dot size indicates the fraction of cells in the population with values greater than 0, dot color represents level of value (Pearson residual normalized expression or gene signature scores for B and C, respectively).

Article

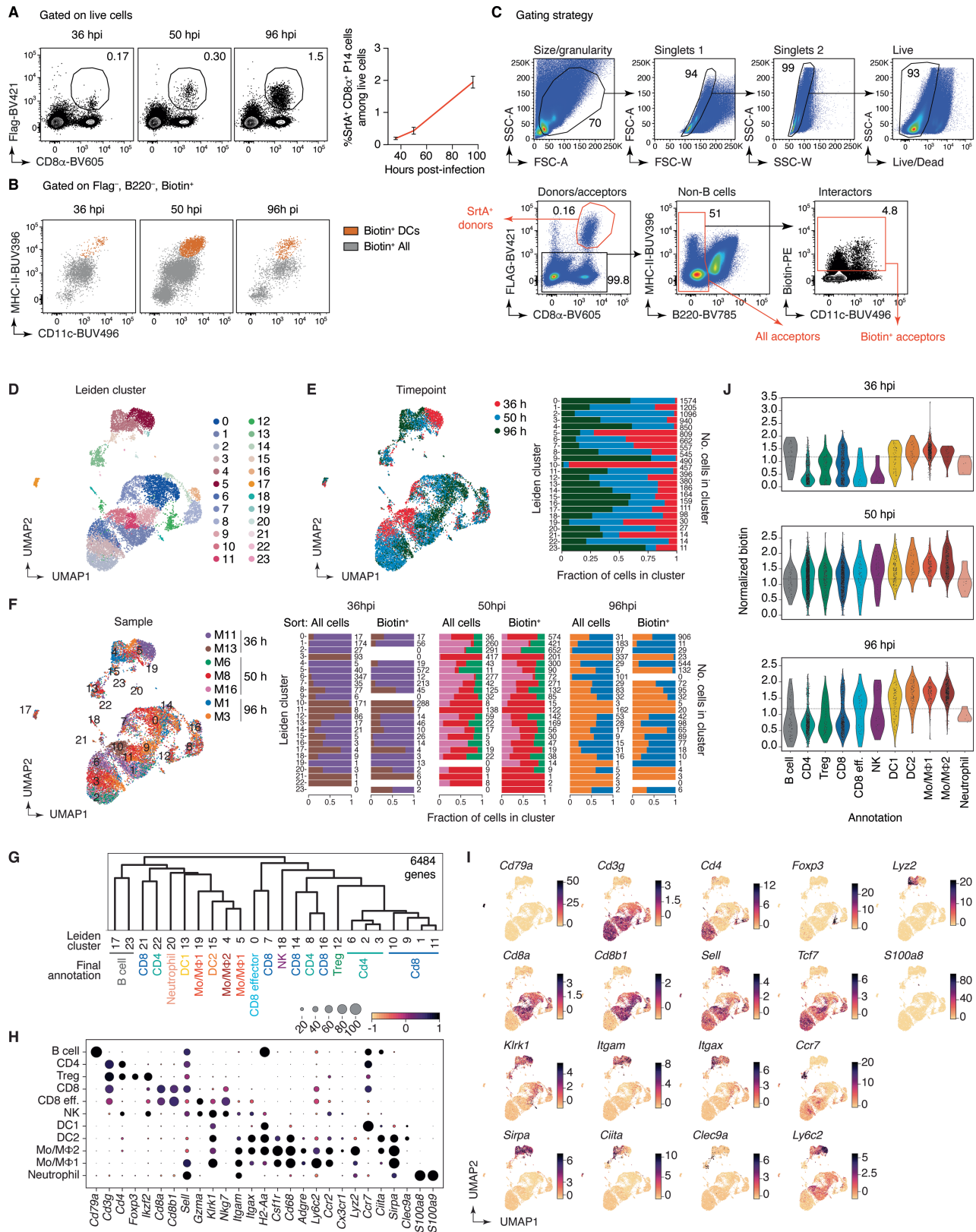


Extended Data Fig. 8 | See next page for caption.

Extended Data Fig. 8 | Analysis of combined scRNA-seq + uLIPSTIC data for CD4⁺ T cells. (A) UMAP for CD4⁺ T cells showing new Leiden sub-clusters and expression of selected marker genes in each cluster ($n = 915$). (B) Dot plot of marker genes for each annotated subset of CD4⁺ T cells. Dot size indicates the fraction of cells in the cluster with Pearson residual normalized expression greater than 0, dot color represents level of expression. (C) Bar plot indicating CD4 Leiden cluster composition by biological replicate, cluster size indicated at the top of each bar. (D) Spearman correlation values, in increasing order, for uLIPSTIC signal and normalized expression of a gene, calculated separately for cells from each biological replicate, indicating consistency across mice. (E) Spearman correlation values, in increasing order, for uLIPSTIC signal and normalized expression of a gene, calculated when removing Tfh-like and naïve/conventional T cells (Leiden CD4 sub-clusters 0 and 1). (F–I) Correlation between acquisition of uLIPSTIC label and expression of CD103 and selected gene signatures by CD4⁺ IELs. (F) Flow cytometry plots show uLIPSTIC signal and

CD103 expression in one control *Rosa26*^{uLIPSTIC/WT} and three *Vil1-Cre.Rosa26*^{uLIPSTIC/WT} mice treated as in Fig. 3g. (G) Gene signatures from the MSigDB “canonical pathways” (M2.CP) database showing significant positive association with normalized biotin signal in scRNA-seq analysis over all CD4⁺ T cells. Plots show Spearman’s ρ value for each signature. (H) Correlation between acquisition of uLIPSTIC signal by CD4⁺ T cells (shown for all T cells and excluding Tfh-like and naïve/Tconv clusters) and expression of the Biocarta CTL gene signature. Trend line and error are for linear regression with 95% confidence interval, Spearman’s ρ and two-sided P-value are listed. (I) Correlation between acquisition of uLIPSTIC signal by CD4⁺ T cells (shown for T cells excluding Tfh-like and naïve/Tconv clusters) and expression of gene signatures up and downregulated as epithelial T cells transition from Tconv (CD4⁺CD103⁺CD8 $\alpha\alpha'$) to CD4⁺ IEL (CD4⁺CD103⁺CD8 $\alpha\alpha'$) phenotypes (signatures based on data from Bilate et al.⁶). Trend line and error are for linear regression with 95% confidence interval, Spearman’s ρ and two-sided P-value are listed.

Article

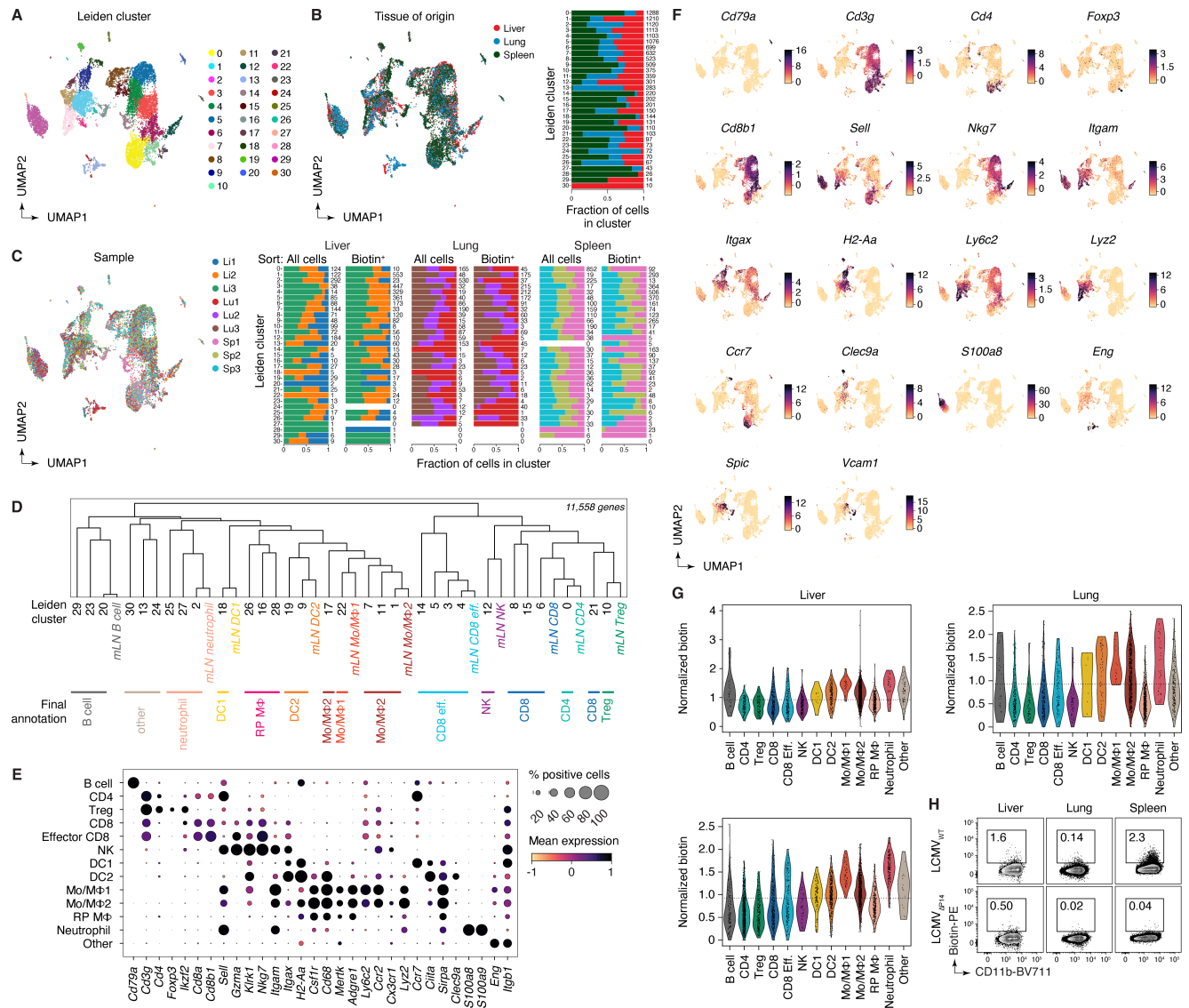


Extended Data Fig. 9 | See next page for caption.

Extended Data Fig. 9 | Using uLIPSTIC to study CD8⁺ T cell priming during acute systemic LCMV infection. (A) *Left*, adoptively transferred LCMV-specific P14 CD8⁺ T cells infiltrated the mediastinal (m)LN of LCMV-infected *Rosa26*^{uLIPSTIC/uLIPSTIC} hosts as early as 36 hpi. *Right*, fraction of P14 cells in total lymphocytes at the indicated timepoint. Data for ten mice per timepoint from three independent experiments, bar plots show mean ± SEM. (B) uLIPSTIC labeling of the P14-interactome (“Biotin⁺ All” in grey) showed that DCs (“Biotin⁺ DCs,” in orange) make up only a fraction of all interacting cells. (C) Sorting strategy for the scRNA-seq experiment. Immune cells—excluding B cells—were sorted both in an unbiased and biased manner, enriching for biotin⁺ acceptor cells and Flag⁺ donor cells using distinct hashtag oligos for downstream classification. Two-three independent samples per timepoint were sorted and stained with different hashtag oligos for downstream identification. (D–J) scRNA-seq analysis of the immune interactome of P14 CD8⁺ T cells in the mLN during acute LCMV infection. (D) UMAP colored by Leiden clustering of the entire scRNA-seq/uLIPSTIC dataset (n = 11,846 cells). (E) *Left*, UMAP colored by timepoint. *Right*, bar plot indicating cluster composition by timepoint,

cluster size indicated at the right of each bar the right. (F) *Left*, UMAP colored by biological replicate. *Right*, bar plot indicating cluster composition by biological replicate, separated by whether the sample was sorted as total mLN cells or biotin-enriched mLN cells, as specified in (C). The cluster size is indicated at the right of each bar. (G) Dendrogram representing transcriptional similarities among clusters. Differentially expressed genes were identified for each cluster ($\log_{2}FC > 1$, FDR < 0.01, see Methods), and normalized expression of all such genes (6,484 genes total), averaged per cluster, was used for the hierarchical clustering analysis that produced the dendrogram. Final annotation clusters shown in Fig. 5 are indicated below the Leiden cluster numbers. (H) Dot plot of marker genes indicating their level of expression in each cell type annotation. Dot size indicates the fraction of cells in the cluster with Pearson residual normalized expression greater than 0, dot color represents level of expression. (I) UMAPs showing normalized gene expression levels for selected marker genes. (J) Violin plot showing levels of normalized uLIPSTIC signal for each cell type annotation, separated by timepoint and excluding P14 donor cells (high FLAG).

Article



Extended Data Fig. 10 | Analysis of combined scRNA-seq + uLIPSTIC data for LCMV tissues (profiled at 96 hpi). (A) UMAP colored by Leiden clustering of the entire scRNA-seq/uLIPSTIC dataset ($n = 12,324$ cells). (B) Left, UMAP colored by tissue type. Right, bar plot indicating cluster composition by tissue, cluster size indicated at the right of each bar. (C) Left, UMAP colored by biological replicate. Right, bar plot indicating cluster composition by biological replicate, separated by whether the sample was unsorted cells or sorted as biotin-enriched cells. The cluster size is indicated at the right of each bar. (D) Dendrogram representing transcriptional similarities among tissue Leiden clusters with annotations from the mLN data. Normalized expression of all genes in the LCMV datasets (11,558 genes total), averaged per Leiden cluster for the tissue data and averaged per annotation for the mLN data, was used for the hierarchical clustering analysis that produced the dendrogram. Final annotation clusters shown in Fig. 5 are indicated below the Leiden cluster numbers. (E) Dot plot of marker genes indicating their level of expression in each cell type annotation. Dot size indicates the fraction of cells in the population with Pearson residual normalized expression greater than 0, dot color represents level of expression. (F) UMAP plots showing normalized gene expression levels for selected marker genes characteristic of the final annotation clusters. (G) Violin plot showing levels of normalized uLIPSTIC signal for each cell type annotation, separated by tissue type and excluding P14 donor cells (high FLAG). (H) uLIPSTIC labeling of MHC-II^{hi} monocytes/macrophages (Mo/MΦ2) in organs of mice treated as in Fig. 5a but infected with either LCMV_{WT} or LCMV_{P14}, analyzed at 96 hpi. Data from one experiment with each symbol representing one mouse, P-values were calculated using two-tailed Student's t-test.

indicated below the Leiden cluster numbers. (E) Dot plot of marker genes indicating their level of expression in each cell type annotation. Dot size indicates the fraction of cells in the population with Pearson residual normalized expression greater than 0, dot color represents level of expression. (F) UMAP plots showing normalized gene expression levels for selected marker genes characteristic of the final annotation clusters. (G) Violin plot showing levels of normalized uLIPSTIC signal for each cell type annotation, separated by tissue type and excluding P14 donor cells (high FLAG). (H) uLIPSTIC labeling of MHC-II^{hi} monocytes/macrophages (Mo/MΦ2) in organs of mice treated as in Fig. 5a but infected with either LCMV_{WT} or LCMV_{P14}, analyzed at 96 hpi. Data from one experiment with each symbol representing one mouse, P-values were calculated using two-tailed Student's t-test.

Reporting Summary

Nature Portfolio wishes to improve the reproducibility of the work that we publish. This form provides structure for consistency and transparency in reporting. For further information on Nature Portfolio policies, see our [Editorial Policies](#) and the [Editorial Policy Checklist](#).

Statistics

For all statistical analyses, confirm that the following items are present in the figure legend, table legend, main text, or Methods section.

n/a Confirmed

- The exact sample size (n) for each experimental group/condition, given as a discrete number and unit of measurement
- A statement on whether measurements were taken from distinct samples or whether the same sample was measured repeatedly
- The statistical test(s) used AND whether they are one- or two-sided
Only common tests should be described solely by name; describe more complex techniques in the Methods section.
- A description of all covariates tested
- A description of any assumptions or corrections, such as tests of normality and adjustment for multiple comparisons
- A full description of the statistical parameters including central tendency (e.g. means) or other basic estimates (e.g. regression coefficient) AND variation (e.g. standard deviation) or associated estimates of uncertainty (e.g. confidence intervals)
- For null hypothesis testing, the test statistic (e.g. F , t , r) with confidence intervals, effect sizes, degrees of freedom and P value noted
Give P values as exact values whenever suitable.
- For Bayesian analysis, information on the choice of priors and Markov chain Monte Carlo settings
- For hierarchical and complex designs, identification of the appropriate level for tests and full reporting of outcomes
- Estimates of effect sizes (e.g. Cohen's d , Pearson's r), indicating how they were calculated

Our web collection on [statistics for biologists](#) contains articles on many of the points above.

Software and code

Policy information about [availability of computer code](#)

Data collection	<input type="checkbox"/> Data collection code was not used in this study
Data analysis	<input type="checkbox"/> Computational analysis of single-cell RNA sequencing data used Python v. 3.9.2 and 3.9.11; CellRanger v6.0.1 and v7.0.1; and R v. 4.0.3 for q-value pathway analysis. Non-single cell RNA sequencing graphs were plotted using Prism v.9, and edited for appearance using Adobe Illustrator 27.1.1. Statistical tests were performed in Prism v.9. Flow cytometry data was analyzed using FlowJo v10. Structural modeling of the Thy1-G5:mSrtA interaction was performed using AlphaFold 2; COOT v. 0.8.9.2; the GalaxyWEB server (https://galaxy.seoklab.org/); CHARMM-GUI (https://www.charmm-gui.org/); ChimeraX v. 1.4; and PyMOL v. 2.4.2.

For manuscripts utilizing custom algorithms or software that are central to the research but not yet described in published literature, software must be made available to editors and reviewers. We strongly encourage code deposition in a community repository (e.g. GitHub). See the Nature Portfolio [guidelines for submitting code & software](#) for further information.

Data

Policy information about [availability of data](#)

All manuscripts must include a [data availability statement](#). This statement should provide the following information, where applicable:

- Accession codes, unique identifiers, or web links for publicly available datasets
- A description of any restrictions on data availability
- For clinical datasets or third party data, please ensure that the statement adheres to our [policy](#)

Processed scRNA-seq data, python code and Jupyter notebooks used for data analysis are available at <https://github.com/pritykinlab/ulipstic-analysis>. Single-cell RNA-seq data are available at GEO under accession number GSE253000.

Research involving human participants, their data, or biological material

Policy information about studies with [human participants or human data](#). See also policy information about [sex, gender \(identity/presentation\), and sexual orientation](#) and [race, ethnicity and racism](#).

Reporting on sex and gender

N/A

Reporting on race, ethnicity, or other socially relevant groupings

N/A

Population characteristics

N/A

Recruitment

N/A

Ethics oversight

N/A

Note that full information on the approval of the study protocol must also be provided in the manuscript.

Field-specific reporting

Please select the one below that is the best fit for your research. If you are not sure, read the appropriate sections before making your selection.

Life sciences Behavioural & social sciences Ecological, evolutionary & environmental sciences

For a reference copy of the document with all sections, see nature.com/documents/nr-reporting-summary-flat.pdf

Life sciences study design

All studies must disclose on these points even when the disclosure is negative.

Sample size

No statistical methods were used to determine sample size. Numbers of mice per group within each independent experiment were limited to numbers typically used in the field. The cell line experiment was performed twice with triplicate technical replicates, as is the standard for such assays.

Data exclusions

No data points were excluded from the analysis.

Replication

Experiments were performed multiple times independently, as described in the figure legends, with the exception of scRNA-seq experiments, where all biological replicates were performed simultaneously to prevent batch effects, and the XXXXXXXXX experiment, which was performed only once.

Randomization

Littermate mice were used to control for litter, cage, and age effects. Mice were divided stochastically (but without a specific randomization procedure) between experimental groups. Randomization is not relevant for cell line experiments.

Blinding

Experimenters were not blinded to experimental group, since most readouts (e.g. FACS fluorescence intensities) are not subjective.

Reporting for specific materials, systems and methods

We require information from authors about some types of materials, experimental systems and methods used in many studies. Here, indicate whether each material, system or method listed is relevant to your study. If you are not sure if a list item applies to your research, read the appropriate section before selecting a response.

Materials & experimental systems

n/a	Involved in the study
<input type="checkbox"/>	<input checked="" type="checkbox"/> Antibodies
<input type="checkbox"/>	<input checked="" type="checkbox"/> Eukaryotic cell lines
<input checked="" type="checkbox"/>	<input type="checkbox"/> Palaeontology and archaeology
<input type="checkbox"/>	<input checked="" type="checkbox"/> Animals and other organisms
<input checked="" type="checkbox"/>	<input type="checkbox"/> Clinical data
<input checked="" type="checkbox"/>	<input type="checkbox"/> Dual use research of concern
<input checked="" type="checkbox"/>	<input type="checkbox"/> Plants

Methods

n/a	Involved in the study
<input checked="" type="checkbox"/>	<input type="checkbox"/> ChIP-seq
<input type="checkbox"/>	<input checked="" type="checkbox"/> Flow cytometry
<input checked="" type="checkbox"/>	<input type="checkbox"/> MRI-based neuroimaging

Antibodies

Antibodies used

- Rat monoclonal anti-MHC-II BV421 (clone M5/114.15.2) BioLegend 107632
 Rat monoclonal anti-MHC-II FITC (clone M5/114.15.2) BioLegend 107606
 Rat monoclonal anti-MHC-II AF700 (clone M5/114.15.2) Invitrogen 56-5321-82
 Rat monoclonal anti-MHC-II BUV395 (clone 2G9) BD Biosciences 743876
 Hamster monoclonal anti-CD11c BUV496 (clone N418) BD Biosciences 750450
 Armenian hamster monoclonal anti-CD11c APC (clone N418) BioLegend 117310
 Rat monoclonal anti-CD11b BV711 (clone M1/70) BioLegend 101242
 Mouse monoclonal anti-XCR1 PerCP-Cy5.5 (clone ZET) BioLegend 148208
 Mouse monoclonal anti-biotin PE (clone Bio3-18E7) Miltenyi Biotec 130-090-756
 Mouse monoclonal anti-biotin APC (clone Bio3-18E7) Miltenyi Biotec 130-113-288
 Rat monoclonal anti-DYKDDDK (FLAG) APC (clone L5) BioLegend 637308
 Rat monoclonal anti-DYKDDDK (FLAG) BV421 (clone L5) BioLegend 637321
 Mouse monoclonal anti-CD90.1 (Thy-1.1) BV421 (clone OX-7) BioLegend 202529
 Mouse monoclonal anti-CD90.1 (Thy-1.1) PE-Cy7 (clone OX-7) BioLegend 202518
 Armenian hamster monoclonal anti-CD3? BV785 (clone 145-2C11) BioLegend 100355
 Mouse monoclonal anti-CD19 BV605 (clone HIB19) BioLegend 302244
 Rat monoclonal anti-B220 BUV395 (clone RA3-6B2) BD Biosciences 563793
 Rat monoclonal anti-B220 FITC (clone RA3-6B2) BioLegend 103206
 Rat monoclonal anti-B220 BV785 (clone RA3-6B2) BioLegend 103245
 Rat monoclonal anti-NK1.1 BV785 (clone PK136) BioLegend 108749
 Rat monoclonal anti-F4/80 PE-Cy7 (clone BM8) BioLegend 123114
 Rat monoclonal anti-F4/80 BUV805 (clone T45-2342) BD Biosciences 749282
 Rat monoclonal anti-CD4 BV785 (clone RM4-5) BioLegend 100551
 Rat monoclonal anti-CD4 PE-Cy7 (clone GK1.5) Invitrogen 25-0041-81
 Rat monoclonal anti-CD4 BUV496 (clone GK1.5) BD Biosciences 612952
 Rat monoclonal anti-CD4 AF700 (clone RM4-5) BD Biosciences 557956
 Rat monoclonal anti-CD8 BUV805 (clone 53-6.7) BD Biosciences 612898
 Rat monoclonal anti-CD8 BV711 (clone H35-17.2) BD Biosciences 740761
 Rat monoclonal anti-CD45 FITC (clone 30-F11) BD Biosciences 553080
 Rat monoclonal anti-CD45 AF700 (clone 30-F11) BioLegend 103128
 Rat monoclonal anti-CD45 BUV395 (clone 30-F11) BD Biosciences 564279
 Mouse monoclonal anti-CD45.1 PE-Cy7 (clone A20) BioLegend 110730
 Mouse monoclonal anti-CD45.2 FITC (clone 104) BioLegend 109816
 Mouse monoclonal anti-CD45.2 PE-Cy7 (clone 104) BioLegend 109830
 Rat monoclonal anti-CD86 BV605 (clone GL1) BioLegend 105037
 Rat monoclonal anti-CD86 AF488 (clone GL1) BioLegend 105018
 Rat monoclonal anti-CD40 BV421 (clone 3/23) BD Biosciences 562846
 Armenian hamster monoclonal anti-CD69 FITC (clone H1.2F3) Invitrogen 11-0691-85
 Armenian hamster monoclonal anti-CD80 PerCP-Cy5.5 (clone 16-10A1) BioLegend 104722
 Armenian hamster monoclonal anti-TCR APC-eFluor780 (clone H57-597) Invitrogen 47-5961-82
 Hamster monoclonal anti-TCR BUV395 (clone H57-597) BD Biosciences 742485
 Armenian hamster monoclonal anti-CD103 BV785 (clone 2E7) BioLegend 121439
 Rat monoclonal anti-FOXP3 APC (clone FJK-16s) Invitrogen 17-5773-82
 Rat monoclonal anti-FOXP3 PerCP-Cy5.5 (clone FJK-16s) Invitrogen 45-5773-82
 Rat monoclonal anti-FOXP3 FITC (clone FJK-16s) Invitrogen 11-5773-82
 Armenian hamster monoclonal anti-JAML AF647 (clone 4E10) BioLegend 128506
 Armenian hamster monoclonal anti-TCR / PerCP-eFluor710 (clone GL3) Invitrogen 46-5711-82
 Rat monoclonal anti-CD326 (Ep-CAM) BV605 (clone G8.8) BioLegend 118227
 Rat monoclonal anti-CD8a Biotin (clone 53-6.7) BioLegend 100704
 Rat monoclonal anti-CD11b Biotin (clone M1/70) BioLegend 101204
 Mouse monoclonal anti-NK1.1 Biotin (clone PK136) BioLegend 108704
 Rat monoclonal anti-CD25 Biotin (clone 7D4) BD Biosciences 553070
 Armenian hamster monoclonal anti-CD11c Biotin (clone N418) BioLegend 117304
 Rat monoclonal anti-TER-119 Biotin (clone TER-119) BD Biosciences 553672
 Rat monoclonal anti-B220 Biotin (clone RA3-6B2) BD Biosciences 553086
 Rat monoclonal anti-CD4 Biotin (clone GK1.5) BioLegend 100404
 Armenian hamster monoclonal anti-CD40L (clone MR1) BioXCell BE0017-1
 Rat monoclonal anti-MHC-II (clone M5/114) BioXCell BE0108

Armenian hamster monoclonal anti-JAML (clone 4E10) BioLegend 128502
 Rat monoclonal anti-Ly-6G/Ly-6C FITC (clone RB6-8C5) Invitrogen 11-5931-82
 Rat monoclonal anti-Ly-6G APC (clone 1A8) BioLegend 127614
 Rat monoclonal anti-Ly-6C FITC (clone HK1.4) BioLegend 128005
 Rat monoclonal anti-CD279 (PD-1) PE-Cy7 (clone RMP1-30) BioLegend 109109
 Rat monoclonal anti-CD279 (PD-1) APC-Cy7 (clone 29F.1A12) BioLegend 135224
 Rat monoclonal anti-CD185 (CXCR5) BV650 (clone L138D7) BioLegend 145517
 Mouse monoclonal anti-CX3CR1 APC (clone SA011F11) BioLegend 149007
 TotalSeq-C0301 Rat monoclonal anti-CD45 (clone 30-F11) and anti-MHC-I (clone M1/42) Hashtag 1 BioLegend 155861
 TotalSeq-C0302 Rat monoclonal anti-CD45 (clone 30-F11) and anti-MHC-I (clone M1/42) Hashtag 2 BioLegend 155863
 TotalSeq-C0303 Rat monoclonal anti-CD45 (clone 30-F11) and anti-MHC-I (clone M1/42) Hashtag 3 BioLegend 155865
 TotalSeq-C0304 Rat monoclonal anti-CD45 (clone 30-F11) and anti-MHC-I (clone M1/42) Hashtag 4 BioLegend 155867
 TotalSeq-C0305 Rat monoclonal anti-CD45 (clone 30-F11) and anti-MHC-I (clone M1/42) Hashtag 5 BioLegend 155869
 TotalSeq-C0306 Rat monoclonal anti-CD45 (clone 30-F11) and anti-MHC-I (clone M1/42) Hashtag 6 BioLegend 155871
 TotalSeq-C0307 Rat monoclonal anti-CD45 (clone 30-F11) and anti-MHC-I (clone M1/42) Hashtag 7 BioLegend 155873
 TotalSeq-C0308 Rat monoclonal anti-CD45 (clone 30-F11) and anti-MHC-I (clone M1/42) Hashtag 8 BioLegend 155875
 TotalSeq-C0436 Mouse monoclonal anti-biotin (clone 1D4-C5) BioLegend 409011
 TotalSeq-C1129 Rat monoclonal anti-DYKDDDDK (FLAG) (clone L5) BioLegend 637335

Validation

All antibodies validated on the manufacturers' websites.

Eukaryotic cell lines

Policy information about [cell lines and Sex and Gender in Research](#)

Cell line source(s)	293T adherent cells (ATCC Cat# CRL-3216) were used for protein expression and binding assays. LCMV strains were produced in BHK-21 cells (ATCC, Cat# CCL-10) and infectious viral titers were assessed by plaque assays on Vero E6 (ATCC, Cat# CRL-1586 VERO C1008) monolayers. All lines were obtained directly from ATCC.
Authentication	Cell lines were only used for protein expression and virus production only, which were confirmed successful as per the experimental data. No further authentication was performed beyond that provided by the vendor.
Mycoplasma contamination	293T lines tested negative for mycoplasma. BHK-21 and Vero E6 lines were not tested after receipt from the vendor but are were used at low passage numbers (3-4 passages).
Commonly misidentified lines (See ICLAC register)	No commonly misidentified cell lines were used.

Animals and other research organisms

Policy information about [studies involving animals; ARRIVE guidelines](#) recommended for reporting animal research, and [Sex and Gender in Research](#)

Laboratory animals	5-12 week old adult male and female mice on the C57BL/6J background were used. See 'mice' section in the methods for further details. Mice were housed at 72 °F (22.2 °C) and 30–70% humidity in a 12-h light/dark cycle with ad libitum access to food and water.
Wild animals	The study did not involve wild animals.
Reporting on sex	Both sexes of mice were used throughout the study. No significant differences were noted between sexes.
Field-collected samples	The study did not involve samples collected from the field.
Ethics oversight	All protocols were approved by the Rockefeller University and Mount Sinai School of Medicine Institutional Animal Care and Use Committees (protocol numbers 22058-H and IACUC-2018-0018/PROTO201900609, respectively).

Note that full information on the approval of the study protocol must also be provided in the manuscript.

Plants

Seed stocks	Report on the source of all seed stocks or other plant material used. If applicable, state the seed stock centre and catalogue number. If plant specimens were collected from the field, describe the collection location, date and sampling procedures.
Novel plant genotypes	Describe the methods by which all novel plant genotypes were produced. This includes those generated by transgenic approaches, gene editing, chemical/radiation-based mutagenesis and hybridization. For transgenic lines, describe the transformation method, the number of independent lines analyzed and the generation upon which experiments were performed. For gene-edited lines, describe the editor used, the endogenous sequence targeted for editing, the targeting guide RNA sequence (if applicable) and how the editor was applied.
Authentication	Describe any authentication procedures for each seed stock used or novel genotype generated. Describe any experiments used to assess the effect of a mutation and, where applicable, how potential secondary effects (e.g. second site T-DNA insertions, mosaicism, off-target gene editing) were examined.

Flow Cytometry

Plots

Confirm that:

- The axis labels state the marker and fluorochrome used (e.g. CD4-FITC).
- The axis scales are clearly visible. Include numbers along axes only for bottom left plot of group (a 'group' is an analysis of identical markers).
- All plots are contour plots with outliers or pseudocolor plots.
- A numerical value for number of cells or percentage (with statistics) is provided.

Methodology

Sample preparation

For flow cytometry of lymph node cells, lymph nodes were collected into microfuge tubes with 500 µl HBSS (Gibco) supplemented with CaCl₂, MgCl₂, and collagenase D at 400 U ml⁻¹ (Roche). pLNs were cut into small pieces and incubated for 30 min at 37 °C. After digestion, tissue was forced 5 times through a 21-gauge needle and filtered through a 70 µm strainer into a 15 ml falcon tube with PBS supplemented with 0.5% BSA and 2 mM EDTA (PBE).

For flow cytometry of immune cells from other tissues:

Intraepithelial leukocytes: Small intestines were harvested and washed in PBS. Peyer's patches were surgically removed and the intestine was segmented in ~1 cm pieces prior to incubation with 1 mM dithiothreitol for 10 min at room temperature followed by addition of 30 mM EDTA and incubation for 30 min at 37°C. Intraepithelial cells were recovered from the supernatant of dithiothreitol and EDTA washes and mononuclear cells were isolated by collecting the middle ring after 40% and 80% gradient Percoll centrifugation.

Bone marrow cells: Punctured tibiae and femurs were centrifuged at up to 10,000 × G for 10 s, then treated with ACK red blood cell lysing buffer.

Immune cells from the kidney, lungs, spleen, thymus and liver: Tissue was cut into pieces and incubated in 1.5 ml HBSS supplemented with collagenase D at 400 U ml⁻¹, 0.1 mg ml⁻¹ DNase1 and 0.8 mg ml⁻¹ dispase 1 for 30 min at 37°C. After digestion, tissue was forced 5 times through a 21-gauge needle and filtered through a 70 µm strainer into a 15 ml falcon tube with PBE. Red-blood cells were lysed with ACK buffer and the resulting cell suspensions were filtered through a 70-µm mesh into PBE.

Immune cells from the brain: Mice were anesthetized and perfused transcardially with 10 ml ice-cold HBSS without Ca²⁺ and Mg²⁺ and the brains were removed and kept in ice-cold HBSS before further process. To stain and discard CD45+ cells from blood vessels for downstream analysis, anti-CD45 antibodies were retro-orbitally injected 15 min before perfusion. The entire brain was minced by mashing through a 150 µm cell strainer and the strainer was washed thoroughly by ice-cold HBSS to collect as many cells as possible. Minced tissues were spun down at 290 g for 5 min at 4°C to discard the supernatant and digested in 2 ml of Digestion solution (2 mg ml⁻¹ collagenase D, 25 mM HEPES, 1 mM sodium pyruvate, 14 µg ml⁻¹ DNase 1 in HBSS) for 20 min at 37°C without shaking. Digestion was stopped by adding 2 ml ice-cold HBSS and the tissues were homogenized with syringes fitted with 21G, 25G, and 27G needles, sequentially. The homogenates were filtered through a 70 µm mesh and spun down at 420 g for 7 min at 4°C to discard the supernatant. The pellets were resuspended in 37% Percoll solution in HBSS and centrifuged at 500 g for 10 min at room temperature to discard supernatant with a myelin layer. The cells in pellets were washed and resuspended in HBSS for further analysis.

Instrument

BD FACSymphony A5 cytometer for analysis and BD FACSAria II/III and FACSymphony S6 for cell sorting.

Software

FlowJo v.10 software

Cell population abundance

Cell sorting was performed for Chromium single cell RNA sequencing. Cell population abundance was confirmed by quantification of hashtag oligos used to identify different samples and cell types.

Gating strategy

Gating strategy for main populations are shown in Extended Data Figure 1C and Extended Data Figure 6A.
Gating strategy for cell sorting for single cell RNA sequencing is shown in Extended Data Figure 6C and Extended Data Figure 9C.

- Tick this box to confirm that a figure exemplifying the gating strategy is provided in the Supplementary Information.